2
Electrons in sp^2 Nanocarbons

Usually Raman spectra only involve phonons explicitly, being independent of the laser energy used to excite the Raman spectra and the electronic transitions in the material (to the extent that the electron–phonon interaction is weak). Furthermore, the usual Raman scattering signal is weak. However, the scattering efficiency gets much larger and the Raman signal much stronger when the laser energy matches the energy between optically allowed electronic transitions in the material. This intensity enhancement process is called resonance Raman scattering (RRS) [91]. Under the RRS regime, the resonance Raman intensity is further enhanced by the large density of electronic states (DOS) available for the optical transitions. This large density of states is especially important for one-dimensional systems, which have singularities in their density of states at the energy onset of an allowed optical transitions.

This chapter has the goal of reviewing the important concepts needed for understanding the Raman spectroscopy of sp^2 nanocarbons, making a link between molecular and solid state science. Due to the peculiar π-electron structure (delocalized p_z orbitals, as discussed in Sections 1.3 and 2.2.2), the Raman spectroscopic response in sp^2 nanocarbons depends strongly on their electronic structure due to the ubiquitous resonance processes that dominate their inelastic scattering of light. For this reason, it is important to review the electronic properties of these systems.

We start by reviewing the basic concepts relevant to the electronic energy levels of isolated molecules and what happens when these molecules are assembled in the solid state. In Section 2.1 we present the one-electron system for the hydrogen atom and then move to more and more complex systems, discussing the formation of molecular orbitals and finally building the transition to solid state systems in Section 2.1.5, and to sp^2 nanocarbon systems in particular (Sections 2.2 and 2.3). Here both the molecular orbital theory (bonding and antibonding states) and the valence bonding theory (hybridization) are introduced and, while the discussion of the intermixing may not be fully rigorous, it is useful for gaining an understanding of sp^2 carbon systems. In Section 2.2.1 we present the crystal structure of graphene, which is followed by the tight-binding model for the π-band electronic structure for monolayer graphene in Section 2.2.2. The π-bands extend over an energy range that goes from the Fermi point up to the ultra-violet, and the π-bands are thus responsible for all transport and optical phenomena. In Section 2.2.3 the σ-bands

Raman Spectroscopy in Graphene Related Systems. Ado Jorio, Riichiro Saito, Gene Dresselhaus, and Mildred S. Dresselhaus

ISBN: 978-3-527-40811-5

are reviewed to yield the electronic structure for graphene which contains both π and σ-bands. In flat graphene the σ-bands are not important for optical phenomena. However, when curvature is present, like in the case of carbon nanotubes, σ-π hybridization can occur, with consequences on the optical response. The remaining sections of this chapter extend the picture to few-layer graphene and then to many-layer graphene in Section 2.2.4 and to quantum confinement phenomena occurring in nanoribbons (Section 2.2.5). The effect of quantum confinement on the electronic structure of nanotubes is next discussed in Section 2.3. The structure of carbon nanotubes is introduced in Section 2.3.1 followed by a discussion of the zone-folding procedure (Section 2.3.2) and the density of electronic states (Section 2.3.3), which is important to understand Raman spectroscopy in these materials, as discussed in Section 2.3.4. This chapter ends with a short discussion in Section 2.4 of the physics beyond the simple tight-binding and zone-folding approximations. This final section comes here just as a brief introduction to concepts that will be developed in later chapters.

2.1 Basic Concepts: from the Electronic Levels in Atoms and Molecules to Solids

Before discussing the electronic properties of the crystalline sp^2 systems, we remind the reader about the basic concepts used to describe the electronic levels of a mono-atomic system, the hydrogen atom in Section 2.1.1, and we then move to molecular systems like the H_2 in Section 2.1.2, to NO in Section 2.1.3, and C_2H_2 in Section 2.1.4, and finally leading into the electronic structure of a linear chain of atoms in a periodic lattice in Section 2.1.5. With this procedure, we hope that the reader will feel comfortable when looking at the electron wavefunctions for graphene, carbon nanotubes and other sp^2 carbon systems.

2.1.1 The One-Electron System and the Schrödinger Equation

We start by reviewing the most basic system, that of the hydrogen atom, with one electron of charge $-e$ and mass m orbiting about a nucleus with mass M. The Schrödinger equation for the hydrogen atom [92] is written as:

$$\left[-\frac{\hbar^2}{2\mu}\Delta + V(\boldsymbol{r})\right]\Psi(\boldsymbol{r}) = E\,\Psi(\boldsymbol{r})\,, \tag{2.1}$$

where μ is the reduced mass given by

$$\frac{1}{\mu} = \frac{1}{m} + \frac{1}{M}, \quad \text{or} \quad \mu = \frac{M}{m+M}m\,, \tag{2.2}$$

and the reduced mass is shown in Figure 2.1.

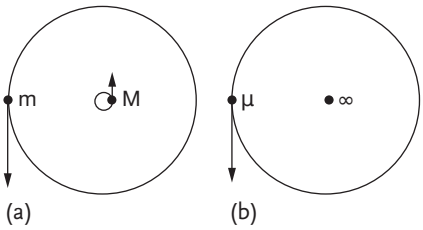

Figure 2.1 Schematic definition of a system with masses m and M in motion (a), and the corresponding reduced mass model system (b), in which a particle with a reduced mass μ is moving around the center of mass, indicated by ∞.

The Coulomb potential $V(\boldsymbol{r})$ for the hydrogen atom has a spherical symmetry which is represented by $r = \sqrt{x^2 + y^2 + z^2}$ and

$$V(\boldsymbol{r}) = -\frac{Ze^2}{4\pi\epsilon_0 r} \,, \tag{2.3}$$

in which Z is the charge on the nucleus ($Z = 1$ for hydrogen), and ϵ_0 is the dielectric constant of vacuum. Since the Hamiltonian has a spherical symmetry around the center, the wavefunction Ψ of Eq. (2.1) can be written as:

$$\Psi(\boldsymbol{r}) = R(r)\Theta(\theta)\Phi(\phi) \,, \tag{2.4}$$

so that Eq. (2.4) can be decomposed into three partial differential equations for $R(r)$, $\Theta(\theta)$ and $\Phi(\phi)$. Since there is no term depending on θ and ϕ in $V(r)$, the solution of Eq. (2.4) simply replaces $\Theta(\theta)$ and $\Phi(\phi)$ by the solution for free space given by the spherical harmonics $Y_\ell^m(\theta, \phi)$. As for the radial part of the wave function $R(r)$, we can solve this by considering Laguerre polynomials. Although we do not go into detail for this solution, the end result for the energy eigenvalues is [92]

$$E_n = -\frac{Z^2}{(4\pi\epsilon_0)^2} \cdot \frac{\mu e^4}{2\hbar} \cdot \frac{1}{n^2} \quad (n = 1, 2, 3, \ldots) \,, \tag{2.5}$$

and $R(r)$ for a given n is expressed by

$$R_{n\ell}(\boldsymbol{r}) = \exp\left(-\frac{Zr}{na_0}\right)\left(\frac{Zr}{a_0}\right)^\ell G_{n\ell}\left(\frac{Zr}{a_0}\right) \,, \tag{2.6}$$

where $G_{n\ell}$ denotes the Laguerre polynomials depending on the variable Zr/a_0 (where a_0 is the Bohr radius, $a_0 = \hbar^2/me^2$). The eigenvalues are characterized by four quantum numbers: the principal quantum number n, the angular momentum quantum number ℓ, the z component of the angular momentum m_ℓ, and the spin of the electron m_s, which are not explicitly written in Eq. (2.5). These quantum numbers assume the following values:

$$n = 1, 2, 3, \ldots \tag{2.7}$$

$$\ell = 0, 1, 2, \ldots, n-1 \,. \tag{2.8}$$

$$m_\ell = -\ell, -\ell+1, \ldots, \ell-1, \ell \,. \tag{2.9}$$

$$m_s = 1/2, -1/2 \,. \tag{2.10}$$

The common designations for the atomic orbitals $s, p, d, \ldots$ correspond to $\ell = 0, 1, 2, \ldots$, respectively.

For the case of carbon $Z = 6$, we predominantly consider the principal quantum numbers $n = 1, 2$ where the $n = 1$ orbital ($1s$) is fully occupied with one spin up and one spin down core electron, and $n = 2$ is half occupied with four electrons with orbitals ($2s, 2p_x, 2p_y$ and $2p_z$) having energies comparable to that of the hydrogen atom. In the lowest energy state, these $n = 2$ electrons occupy the hybridized graphene $sp^2 + p_z$ orbitals, while the four electrons in diamond occupy a symmetric sp^3 hybridized orbital, which is higher in energy at room temperature and under ambient pressure (see also Section 1.1).

2.1.2 The Schrödinger Equation for the Hydrogen Molecule

Now we recall what happens to the electrons when the two H atoms are combined into the H_2 molecule. In the two-electron system of a hydrogen molecule, the Schrödinger equation can be written in matrix form resulting in the solution of a secular equation, written generically as:

$$|\langle \Psi_i | H | \Psi_j \rangle - E \langle \Psi_i | \Psi_j \rangle| = 0 \,, \tag{2.11}$$

where $\langle \Psi_i | H | \Psi_j \rangle$ and $\langle \Psi_i | \Psi_j \rangle$ denote, respectively, the Hamiltonian and overlap matrices for basis functions.[1] Here we consider the hydrogen molecule H_2 and Ψ_i is taken as the hydrogen $1s$ atomic orbital for each H atom. If we adopt the approximation that Ψ_1 and Ψ_2 are orthogonal to each other, then $\langle \Psi_1 | \Psi_2 \rangle = 0$ and the Schrödinger Equation (2.11) yields

$$\begin{cases} E_{1s}\Psi_1 + V_0\Psi_2 = E\Psi_1 \\ V_0\Psi_1 + E_{1s}\Psi_2 = E\Psi_2 \,, \end{cases} \tag{2.12}$$

where E_{1s} is the energy of an unperturbed H atom, and the Hamiltonian matrix element is $V_0 \equiv \langle \Psi_1 | H | \Psi_2 \rangle < 0$. In evaluating the Hamiltonian matrix elements, we should also consider the Coulomb interaction between the two electrons in the Hamiltonian.[2] Here we simply consider that the Coulomb interaction is included

1) Basis functions are atomic orbitals or molecular orbitals that are used by variational principles to obtain the energy by $E = \langle \Psi_i | H | \Psi_j \rangle / \langle \Psi_i | \Psi_j \rangle$.

2) If we use the Hartree–Fock approximation for the Coulomb interaction [93], the interaction further consists of a direct Coulomb term and an exchange term. The exchange term corrects for the overestimation of the direct Coulomb interaction term and arises from the fact that two electrons with the same spin cannot be at the same location in accordance with the Pauli exclusion principle.

in both V_0 and E_{1s}. In matrix form Eq. (2.12) can be written as:

$$\begin{pmatrix} E_{1s} & V_0 \\ V_0 & E_{1s} \end{pmatrix} \begin{pmatrix} \Psi_1 \\ \Psi_2 \end{pmatrix} = E \begin{pmatrix} \Psi_1 \\ \Psi_2 \end{pmatrix} . \tag{2.13}$$

Equation (2.13) can be diagonalized by solving the secular equation[3] (Eq. (2.11)),

$$(E - E_{1s})^2 - V_0^2 = 0 , \tag{2.14}$$

which gives $E = E_{1s} \pm V_0$. The diagonalization can be done by a unitary transformation of the Hamiltonian matrix H given by $U^\dagger H U$, where the unitary matrix U is given by[4]

$$U = (1/\sqrt{2}) \begin{pmatrix} 1 & 1 \\ 1 & -1 \end{pmatrix} . \tag{2.15}$$

The resulting symmetrized eigenvectors will be two molecular orbitals formed by a linear combination of atomic orbitals (LCAOs), given by the symmetric (S) and antisymmetric (AS) combinations [94]

$$\Psi_S = (1/\sqrt{2})(\Psi_1 + \Psi_2) \tag{2.16}$$

$$\Psi_{AS} = (1/\sqrt{2})(\Psi_1 - \Psi_2) . \tag{2.17}$$

The spatial dependence of the electronic wavefunctions for the hydrogen molecule is shown in Figure 2.2, where the symmetric combination $\Psi_S = (1/\sqrt{2})(\Psi_1 + \Psi_2)$ has the lower energy ($E_S = E_{1s} + V_0$), in which V_0 has a negative value, resulting in an enhancement in the probability for finding an electron at the center between the two H atoms. For this reason, this state is usually called the *bonding state*, describing the ground state for the H_2 molecule by occupying two electrons (one spin up, one spin down). The antisymmetric combination $\Psi_{AS} = (1/\sqrt{2})(\Psi_1 - \Psi_2)$, with energy $E_{AS} = E_{1s} - V_0$, is named the *antibonding state* with a node in the wave function at the center between the two H atoms, as shown in Figure 2.2.

2.1.3
Many-Electron Systems: the NO Molecule

In this section we show how the molecular electronic complexity increases when the number of electrons in a diatomic molecule increases. Figure 2.3 shows the schematics of the electronic levels for the heterogeneous diatomic NO molecule [94]. The $1s^2$ levels (core electrons, not shown) lie much lower in energy. These electrons are tightly bound to their respective atoms and do not contribute

3) The secular equation is given by the determinant of the matrix of Eq. (2.13) when it becomes zero. If the determinant is not zero, we get the inverse matrix and multiplying the inverse matrix by Eq. (2.13), we get the meaningless solution of ${}^t(\Psi_1, \Psi_2) = {}^t(0, 0)$.

4) $U^\dagger$ is the transpose and complex conjugate of U. In the case of a unitary matrix, $U^\dagger = U^{-1}$.

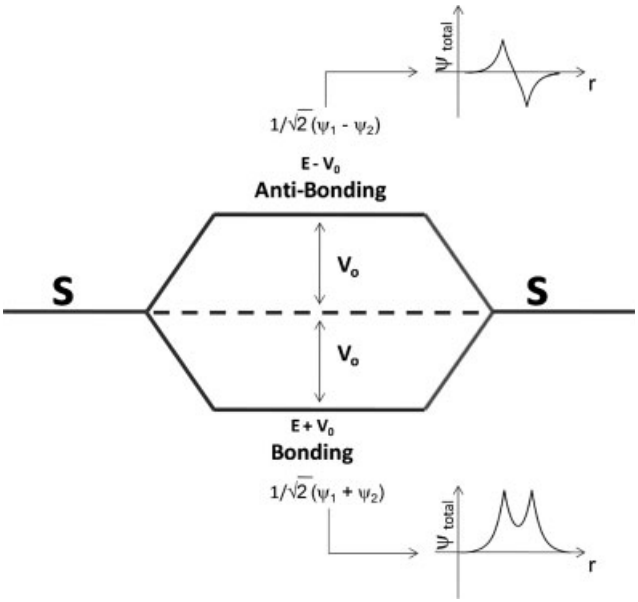

Figure 2.2 Bonding and antibonding molecular levels of the H_2 molecule. The energy separation between the bonding and antibonding orbitals for this symmetric diatomic molecule is given by $2V_0$. The wavefunctions $\Psi(r)$ for the bonding and antibonding states are also shown.

to molecular bonding and molecular properties. The $2s$ electrons form bonding and antibonding states, which are fully occupied by four electrons, similar to the discussion in Section 2.1.2. Next, considering the bonding for the p electrons, the lowest energy is for the $2p_z$ orbitals if we take the z-axis to be along the NO bond direction. The diatomic potential of the NO molecule will break the atomic

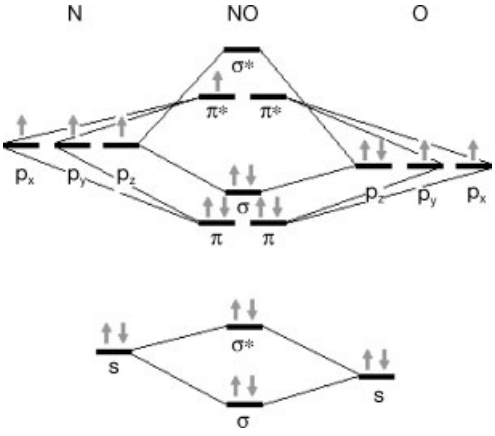

Figure 2.3 Energy levels for the heterogeneous diatomic NO molecule, showing the bonding and antibonding states filled with spin up and spin down electrons (gray).

degeneracy between the $2p_z$ and $2p_{x,y}$ orbitals, while the NO bonding will mix the N and O levels which have the same angular momentum L around the z axis ($L = 0$ for $2s$ and $2p_z$, $L = 1$ for $2p_x$ and $2p_y$), forming bonding and antibonding molecular orbitals,[5] as shown in Figure 2.3 [94]. The 11 electrons pertaining to both the N and O atoms in the $n = 2$ atomic shell (N: $2s^2, 2p^3$ and O: $2s^2, 2p^4$) will fill the five lowest energy levels as shown in Figure 2.3 (accounting for both spin up and spin down states) plus one extra electron in the highest π^* antibonding state. The *highest occupied molecular orbital* and the *lowest unoccupied molecular orbital* are often called the HOMO and LUMO levels, respectively. In the case of NO, π^* is called the singly occupied MO (SOMO). Considering a NO^+ ionized molecule, the highest π^* antibonding state would be empty and become the LUMO level. The p_z-based σ level would represent the HOMO level.

2.1.4
Hybridization: the Acetylene C_2H_2 Molecule

Now we address the problem of hybridization, whereby atomic orbitals mix with each other within an atom to form a chemical bond in a specific direction. Considering Figure 2.3, imagine that the $2s$ level from one atom is closer in energy to the $2p$ level of the other atom. This indeed happens in the CO molecule. Otherwise, imagine that the bonding interaction is strong enough to mix the $2s$ and the $2p_z$ orbitals which have the same symmetry. This happens in some cases where the minimization of energy for the molecular bonding requires an elongation of the electronic wavefunctions to the other atoms. Such an elongation can be represented by the hybridization (mixing) of different atomic orbitals from the same atom, as occurs in the case of acetylene C_2H_2 [31]. Considering the bonding along the x direction, the p_x electrons from the two carbon atoms will be involved in the strongest interatomic bonding. This bonding is called σ bonding, resulting in an elongation of the electronic wavefunctions, as shown in Figure 2.4, where we see a mixing of $|2s\rangle$ and $|2p_z\rangle$ orbitals (s–p hybridization).

The two linear combinations of atomic orbitals (LCAOs) for the H_2C_2 acetylene molecule will be the

$$|sp_a\rangle = \frac{1}{\sqrt{2}}(|2s\rangle + |2p_x\rangle) \tag{2.18}$$

and the

$$|sp_b\rangle = \frac{1}{\sqrt{2}}(|2s\rangle - |2p_x\rangle) \tag{2.19}$$

orbitals, which are elongated along the $+x$ and $-x$ directions, respectively (Figure 2.4), where $|sp_a\rangle$ and $|sp_b\rangle$ are hybridized orbitals for the left and right atoms, respectively. Furthermore the $|sp_a\rangle$ and $|sp_b\rangle$ form the symmetric and antisymmetric combinations $|sp_a\rangle \pm |sp_b\rangle$, respectively, and they are usually named σ and

5) We must consider hybridization of $2s$ and $2p_z$ in the case of NO. This is the reason why σ of $2p_z$ lies higher in energy than π of $2p_x$ and $2p_y$.

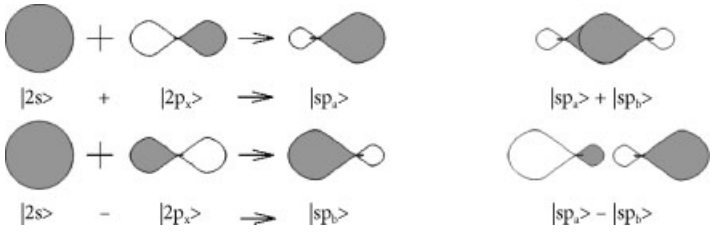

Figure 2.4 Schematics for the sp hybridization and bonding formation [31]. The shading represents the positive value of the wave function $|sp_a\rangle = |2s\rangle + |2p_x\rangle$, where the bond is elongated in the positive direction of x, while the state $|sp_b\rangle = |2s\rangle - |2p_x\rangle$ is elongated in the negative direction. The symmetric ($|sp_a\rangle + |sp_b\rangle$) and antisymmetric ($|sp_a\rangle - |sp_b\rangle$) combinations constitute "bonding" and "antibonding" σ states, respectively.

σ^* states. The σ state is responsible for the strong covalent bonding between two carbon atoms, while the σ^* state is an unoccupied state. The two remaining p_y and p_z electronic states, which are perpendicular to the bonding x direction, form the (weak) so-called π *bonds*, giving rise to the symmetric and antisymmetric orbital combinations that occur in the acetylene molecule HC≡CH [31]. While the symmetric and antisymmetric combinations retain a similarity with the concept of bonding and antibonding orbitals, this connection is not fully correct. In sp^2 carbon systems, hybridization occurs by mixing $2s$, $2p_x$ and $2p_y$ orbitals which make three hybridized orbitals which are elongated to the three nearest neighbor atoms (sp^2 hybridization). The sp^2 hybridized orbitals form three σ (bonding) and three σ^* (antibonding) orbitals. The remaining $2p_z$ form π and π^* orbitals. In the case of sp^2 carbon, π and π^* orbitals correspond to the HOMO and LUMO, respectively. All these concepts are broadly used in the description of the sp^2 nanocarbons.

2.1.5
Basic Concepts for the Electronic Structure of Crystals

Next, we consider the electronic structure of a crystalline solid and attempt to make a connection to the simple concepts used in molecular electronics. The Schrödinger equation for an electron in a crystal is written as [95]:

$$\left[-\frac{\hbar^2}{2m}\nabla^2 + V(\boldsymbol{r})\right]\Psi = E\Psi \,, \tag{2.20}$$

where $V(\boldsymbol{r})$ is now a periodic potential. Since the crystal has a quasi-infinite number of atoms, the number of electronic levels is also quasi-infinite. This generates a quasi-infinite secular equation if we solve for the electronic states by the molecular orbitals method. However, in the case of a crystal, we can use the fact that the crystal is a periodic structure based on a *unit cell* that repeats itself under the lattice vectors labeled by

$$\boldsymbol{R} = n\boldsymbol{a}_1 + m\boldsymbol{a}_2 + l\boldsymbol{a}_3 \,, \tag{2.21}$$

where $\boldsymbol{a}_1$, $\boldsymbol{a}_2$, and $\boldsymbol{a}_3$ are the primitive vectors of the crystal lattice, and n, m, and l are integers. Since the potential $V(\boldsymbol{r})$ is periodic under an $\boldsymbol{R}$ translation ($V(\boldsymbol{r}) = V(\boldsymbol{r} + \boldsymbol{R})$), the solutions to Eq. (2.20) are wave functions that can be written as:

$$\Psi_{\boldsymbol{k}}(\boldsymbol{r}) = e^{i\boldsymbol{k}\cdot\boldsymbol{r}} u_{\boldsymbol{k}}(\boldsymbol{r}) \,, \tag{2.22}$$

where

$$u_{\boldsymbol{k}}(\boldsymbol{r}) = u_{\boldsymbol{k}}(\boldsymbol{r} + \boldsymbol{R}) \,, \tag{2.23}$$

is periodic in accordance with Bloch's Theorem [31, 95]. Figure 2.5 illustrates the formation of Bloch states for a linear chain of atoms, and these Bloch states are defined by the unit cell wavefunction $u_{\boldsymbol{k}}$ (shown as s and p states in Figure 2.5) and e^{ikr} term, which modifies the sign and amplitude as a phase factor. Here $\boldsymbol{k}$ is the wavevector whose length is given by

$$k = 2\pi/\lambda \,, \tag{2.24}$$

where λ is the wavelength of the wavefunction.

Since $\boldsymbol{k}$ is a good quantum number (or a variable that is conserved under translation by $\boldsymbol{R}$), the electronic structures of crystals are displayed in a plot of the electron energy $E_{\boldsymbol{k}}$ vs. electron wavevector $\boldsymbol{k}$, called the *energy dispersion relations*, which consist of quasi-continuous states within a finite region of energy called *electronic energy bands*. From an atomic orbital in a unit cell, we can make a Bloch function and thus produce an energy band which can occupy two electrons per unit cell. Being quasi-continuous, these energy bands account for a quasi-infinity of electronic levels.

The *real coordinate space* (x, y, z) is the space where the atoms are displayed (Figure 1.2), and where the probability for finding an electron with a wave function Ψ is given by taking the square of Ψ, shown in Figure 2.5. The so-called

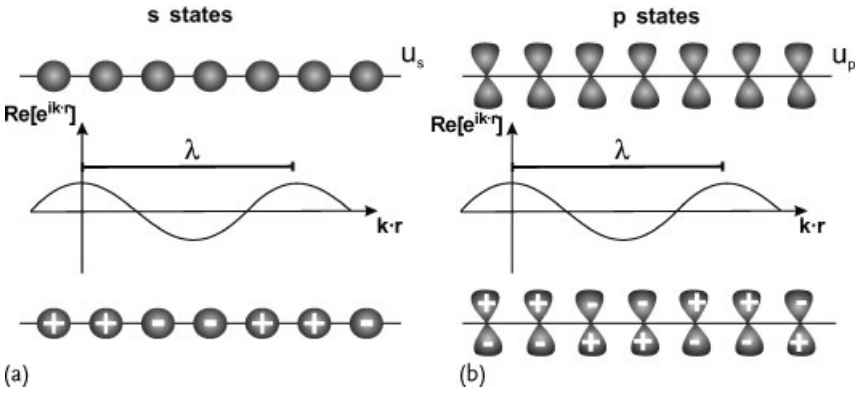

Figure 2.5 Schematic 1D Bloch orbitals formed by s (a) and p_z (b) atomic orbitals. The top shows the wavefunction of each atom, the middle shows the phase of the Bloch orbital e^{ikr}, and the bottom shows the amplitudes of the Bloch orbitals.

reciprocal space (k_x, k_y, k_z) is the space of the wavevectors k for the wavefunctions, and the electronic dispersion relations are representations of the electron energy in reciprocal space.

Consider a hypothetical one-dimensional (1D) crystal made of a quasi-infinite repetition of –N–O–N–O– atoms. Considering $a_{-\mathrm{N-O}}$ as the primitive translation vector in real space, given by the distance between –N–O units, the allowed values for λ (or k, see Eq. (2.24)) are $a_{-\mathrm{N-O}}, 2a_{-\mathrm{N-O}}, 3a_{-\mathrm{N-O}}, \ldots, \mathcal{N}a_{-\mathrm{N-O}}$, where $\mathcal{N}$ is the number of –N–O units in this 1D crystal ($\mathcal{N} \sim 10^{23}$). Compared to the NO molecule in Section 2.1.3, instead of having the 11 electronic levels made of combinations of the N: $2s^2, 2p^3$ and O: $2s^2, 2p^4$ electrons, there will be $11 \times \mathcal{N}$ electronic levels. The energy dispersion relation ($E_{\boldsymbol{k}}$ vs. $\boldsymbol{k}$ plot) in reciprocal space will then be made of 11 energy bands, where the number of energy bands is given by the total number of atomic orbitals in the unit cell. Each energy band accepts $2\mathcal{N}$ electrons or 2 electrons per unit cell. While there will be 11 energy bands (similar to the 11 levels of the NO molecule), the lower 5 energy bands of the 11 energy bands are fully or partially occupied.

Like in the case of molecules, the electronic levels will be filled from the lowest to the highest energy. Because of the odd number of electrons in the unit cell, we expect metallic behavior in which the highest occupied energy band is half occupied. The electronic wavefuction can now change phase when moving along the one-dimensional crystal, with $\mathcal{N}$ wavevectors associated with each electronic band. The energy defining the boundary between the occupied and unoccupied levels is called the *Fermi energy*. If the Fermi energy falls within an electronic band, no energy will be required to take an electron from the occupied to the unoccupied state, and the material is therefore *metallic*.[6] If the Fermi energy falls within an energy gap between the valence (the highest occupied) and the conduction (the lowest unoccupied) energy bands, then the material will be *semiconducting* (with an energy gap on the order of 1 eV) or an *insulator* (gap on the order of 10 eV).[7] Graphene is an interesting system where the energy separation between the valence and conduction bands is zero, imposed by crystal symmetry. Therefore, graphene is a zero gap semiconductor (or metal) with a symmetry-imposed degeneracy between the valence and conduction bands at specific points in two-dimensional (k_x, k_y) reciprocal state [94].

Finally, we define the so-called *Brillouin zone*, which is a symmetry-based unit cell in reciprocal space providing a representation for a wavevector appropriate to a given crystal. The number of allowed $\boldsymbol{k}$ wavevectors inside a Brillouin zone is always limited by the number $\mathcal{N}$ of unit cells in the crystal, where $-\pi/a \leq k \leq \pi/a$ defines the so-called bounding region of the Brillouin zone. Figure 2.5 displays the case for $\lambda = 2a_{-\mathrm{A-B}}$, where $k = \pi/a_{-\mathrm{A-B}}$ at the boundary of the first Brillouin zone. Outside the first Brillouin zone ($k_{\mathrm{out}} > \pi/a$, or $\lambda < 2a_{-\mathrm{A-B}}$) the electronic structure repeats the electronic levels inside the first Brillouin zone with $k = k_{\mathrm{out}} - K$,

6) This would likely happen to this hypothetical NO crystal, since there is one electron in the π^* state in the molecule (see Section 2.1.3).

7) This would likely happen to the hypothetical NO^+ crystal, since the LUMO is empty in the NO^+ molecule (see Section 2.1.3).

where $K = 2\pi/a_{-A-B}$ gives the reciprocal lattice vector in what is called the extended Brillouin zone [95]. This periodicity in reciprocal space is equally applicable to phonons, and we use this periodicity for phonons in Chapter 3. All the concepts briefly summarized in this section are broadly used in the study of sp^2 nanocarbons, as shown in the next sections and chapters. The reader who is not familiar with solid state physics may want to consult a more tutorial solid state physics presentation, such as the introductory text by Kittel [95].

2.2
Electrons in Graphene: the Mother of sp^2 Nanocarbons

The discussion of Section 2.1.5 is now applied to sp^2 nanocarbons. Graphene provides a simple illustration showing that the number of branches in the dispersion relations corresponds to the number of electrons in the unit cell. Graphene has two C atom sites per unit cell, which means 2 sets of 2*s* and 2*p* states (a total of 8 states per unit cell), so that there will be eight electronic energy bands, derived from the 3σ, $3\sigma^*$, 1π and $1\pi^*$ levels. The 8 electrons per unit cell will fill the 4 lower 3σ and 1π bonding energy bands with spin up and spin down electrons, and the 4 higher $3\sigma^*$ and $1\pi^*$ energy bands will be unoccupied.[8)]

2.2.1
Crystal Structure of Monolayer Graphene

The fundamental crystal structure that constitutes the basis for sp^2 carbon nanostructures is graphene, which is a two-dimensional (2D) planar structure based on a unit cell containing two carbon atoms A and B, as shown by the unit vectors $\boldsymbol{a}_1$ and $\boldsymbol{a}_2$ in Figure 2.6a. The carbon atoms in monolayer graphene are located at the vertices of the hexagons where $\boldsymbol{a}_1$ and $\boldsymbol{a}_2$ are unit vectors.

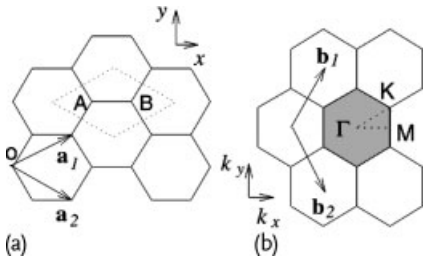

Figure 2.6 (a) The unit cell and (b) Brillouin zone of monolayer graphene are shown as the dotted rhombus and the shaded hexagon, respectively, while $\boldsymbol{a}_i$, and $\boldsymbol{b}_i$, ($i = 1, 2$) are the real space unit vectors and reciprocal lattice vectors, respectively. Energy dispersion relations are usually displayed along the perimeter of the dotted triangle connecting the high symmetry points, Γ, K and M (see inset to Figure 2.7).

8) The electronic energy bands of monolayer graphene are displayed in Figure 2.10.

As shown by Figure 2.6a, the real space unit vectors $\boldsymbol{a}_1$ and $\boldsymbol{a}_2$ of the hexagonal lattice are expressed in Cartesian coordinates as:

$$\boldsymbol{a}_1 = \left(\frac{\sqrt{3}}{2}a, \frac{a}{2}\right), \quad \boldsymbol{a}_2 = \left(\frac{\sqrt{3}}{2}a, -\frac{a}{2}\right), \tag{2.25}$$

where $a = |\boldsymbol{a}_1| = |\boldsymbol{a}_2| = 1.42 \times \sqrt{3} = 2.46\,\text{Å}$ is the lattice constant of monolayer graphene. Likewise, the unit cell in reciprocal space is shown by the shaded hexagon in Figure 2.6b and is described by the unit vectors $\boldsymbol{b}_1$ and $\boldsymbol{b}_2$ of the reciprocal lattice given by

$$\boldsymbol{b}_1 = \left(\frac{2\pi}{\sqrt{3}a}, \frac{2\pi}{a}\right), \quad \boldsymbol{b}_2 = \left(\frac{2\pi}{\sqrt{3}a}, -\frac{2\pi}{a}\right), \tag{2.26}$$

corresponding to a lattice constant of length $4\pi/\sqrt{3}a$ in reciprocal space. The unit vectors $\boldsymbol{b}_1$ and $\boldsymbol{b}_2$ of the reciprocal hexagonal lattice (see Figure 2.6b) are rotated by 30° from the unit vectors $\boldsymbol{a}_1$ and $\boldsymbol{a}_2$ in real space, respectively. The three high symmetry points of the Brillouin zone, Γ, K and M are the center, the corner, and the center of the edge of the hexagon, respectively. Other high symmetry points or lines are along ΓK (named T), KM (named T′) and ΓM (named Σ).

In monolayer graphene, three of the electrons form σ bonds which hybridize in a sp^2 configuration, and the fourth electron of the carbon atom forms the $2p_z$ orbital, which is perpendicular to the graphene plane, and makes π covalent bonds. In Section 2.2.2 we use the tight-binding approximation to treat the covalent π energy bands for graphene which are the simplest for determining the solid state properties of graphene, reflecting the strong coupling of the in-plane carbon atoms. In Section 2.2.3 we review the σ-bands which, together with the π-bands, give the electronic structure of graphene.

2.2.2 The π-Bands of Graphene

In this section we review the derivation of the electronic π-bands of graphene based on the tight-binding model which is used here to provide an approximate description of the π-bands of monolayer graphene because of the very strong in-plane bonding between the carbon atoms in graphene. For a more detailed development of the tight-binding model applied to graphene and other sp^2 carbon systems, see [31, 32].

Within the tight-binding method, the unperturbed eigenvectors are represented by atomic orbitals, and the crystalline potential is treated as a perturbation, thus forming the crystalline electronic states which are represented by Bloch states. Two Bloch functions (Φ_A and Φ_B), constructed from p_z atomic orbitals (φ, with $\Phi_\text{A,B} \propto \sum_R e^{i\boldsymbol{k}\cdot\boldsymbol{R}}\varphi(r-R)$) for the two nonequivalent carbon atoms at A and B sites in Figure 2.6a, provide the basis functions for describing the electronic structure of monolayer graphene (1-LG). The secular equation is derived from a 2×2 Hamilto-

nian matrix, $H_{ij} = \langle \Phi_i | H | \Phi_j \rangle$, containing four matrix elements coupling Φ_A and Φ_B. When we consider only nearest neighbor interactions, then $\mathcal{H}_{AA} = \mathcal{H}_{BB} = \epsilon_{2p}$ for the diagonal matrix elements where ϵ_{2p} is the atomic $2p$ level energy of an isolated carbon atom. For the off-diagonal matrix element $\mathcal{H}_{AB}$, we must consider the three nearest neighbor B atoms relative to an A atom, which are denoted by the vectors $\boldsymbol{R}_1$, $\boldsymbol{R}_2$, and $\boldsymbol{R}_3$ connecting the A atom to its three nearest neighbor B atoms to obtain:

$$\begin{aligned} 2\mathcal{H}_{AB} &= t\left(e^{i\boldsymbol{k}\cdot\boldsymbol{R}_1} + e^{i\boldsymbol{k}\cdot\boldsymbol{R}_2} + e^{i\boldsymbol{k}\cdot\boldsymbol{R}_3}\right) \\ &= t\, f(k)\,, \end{aligned} \tag{2.27}$$

where t is the nearest neighbor transfer integral ($\langle \varphi_A | \mathcal{H} | \varphi_B \rangle$) which is often called $-\gamma_0$ ($t = -\gamma_0$) in the literature, where γ_0 is given a positive value. The function $f(k)$ in Eq. (2.27) is a function of the sum of the phase factors of $e^{i\boldsymbol{k}\cdot\boldsymbol{R}_j}$ ($j = 1, \cdots, 3$). Using the x, y coordinates of Figure 2.6a, $f(k)$ is given by

$$f(k) = e^{ik_x a/\sqrt{3}} + 2e^{-ik_x a/2\sqrt{3}} \cos\left(\frac{k_y a}{2}\right)\,. \tag{2.28}$$

Since $f(k)$ is a complex function, and the Hamiltonian forms a Hermitian matrix, we write $\mathcal{H}_{BA} = \mathcal{H}^*_{AB}$ in which * denotes the complex conjugate. Using Eq. (2.28), the overlap integral matrix, $S_{ij} = \langle \Phi_A | \Phi_B \rangle$ is given by $\mathcal{S}_{AA} = \mathcal{S}_{BB} = 1$, and $\mathcal{S}_{AB} = s\, f(k) = \mathcal{S}^*_{BA}$, with the nearest neighbor overlap integral for p_z wavefunctions, $s = \langle \varphi_A | \varphi_B \rangle$. The explicit forms for $\mathcal{H}$ and $\mathcal{S}$ can be written as:

$$\mathcal{H} = \begin{pmatrix} \epsilon_{2p} & t\, f(k) \\ t\, f(k)^* & \epsilon_{2p} \end{pmatrix}, \quad \mathcal{S} = \begin{pmatrix} 1 & s\, f(k) \\ s\, f(k)^* & 1 \end{pmatrix}\,. \tag{2.29}$$

Solving the secular equation $\det(\mathcal{H} - E\mathcal{S}) = 0$ (where "det" denotes the determinant) and using $\mathcal{H}$ and $\mathcal{S}$ as given in Eq. (2.29), the eigenvalues $E(\boldsymbol{k})$ for the graphene π-bands are obtained as a function $\boldsymbol{k} = (k_x, k_y)$:

$$E(\boldsymbol{k}) = \frac{\epsilon_{2p} \pm t w(\boldsymbol{k})}{1 \pm s w(\boldsymbol{k})}\,, \tag{2.30}$$

where the $+$ signs in the numerator and denominator go together giving the bonding π energy band, and likewise for the $-$ signs, which give the antibonding π^*-band as symmetric and antisymmetric combinations of Φ_A and Φ_B, respectively, (see Section 2.1.2), while the function $w(\boldsymbol{k})$ is given by

$$w(\boldsymbol{k}) = \sqrt{|f(\boldsymbol{k})|^2} = \sqrt{1 + 4\cos\frac{\sqrt{3}k_x a}{2}\cos\frac{k_y a}{2} + 4\cos^2\frac{k_y a}{2}}\,. \tag{2.31}$$

In Figure 2.7, the electronic energy dispersion relations for the π-bands of monolayer graphene are shown throughout the two-dimensional first Brillouin zone and the inset shows the energy dispersion relations along the high symmetry axes along

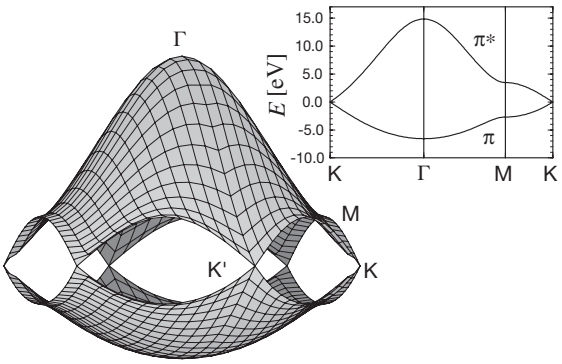

Figure 2.7 The energy dispersion relations for 2D graphite are shown throughout the whole region of the first Brillouin zone [31]. The valence and conduction bands of graphene touch at the points K and K', which are related by time reversal symmetry [94]. The inset shows the energy dispersion $E(k)$ along the high symmetry directions of the triangle ΓMK, shown in Figure 2.6b.

the perimeter of the triangle shown in Figure 2.6b. Here we use values of the parameters $\epsilon_{2p} = 0$, $t = -3.033\,\text{eV}$, and $s = 0.129$ in order to reproduce the first principles calculation of the graphite energy bands [16, 96]. The upper half of the energy dispersion curves describes the π^*-energy "antibonding" band, and the lower half is the π-energy bonding band[9]. Since there are two π electrons per unit cell, these two π electrons fully occupy the lower π-band. Therefore, the π-band is filled by spin up and spin down electrons, while the π^*-band is empty. The upper π^*-band and the lower π-band are degenerate at the K (K') points through which the Fermi energy passes for an undoped monolayer graphene sample.

The existence of a zero gap at the K (K') points comes from the symmetry requirement that the two carbon sites A and B in the hexagonal lattice are distinct but equivalent to each other by symmetry. If the A and B sites had different atoms, such as B and N, then the site energy ϵ_{2p} would be different for B and N, and therefore the calculated energy dispersion would show an energy gap between the π and π^*-bands ($E_g = 3.5\,\text{eV} = \epsilon_{2p}^{\text{B}} - \epsilon_{2p}^{\text{N}}$ for BN).

When the graphene overlap integral s becomes zero, the π and π^*-bands become symmetrical around $E = \epsilon_{2p}$, which can be understood from Eq. (2.30). The energy dispersion relations in the case of $s = 0$ are commonly used as a simple approximation for the electronic structure of a graphene layer near $E = \epsilon_{2p}$:

$$E(k_x, k_y) = \pm t \left\{ 1 + 4\cos\left(\frac{\sqrt{3}k_x a}{2}\right)\cos\left(\frac{k_y a}{2}\right) + 4\cos^2\left(\frac{k_y a}{2}\right) \right\}^{1/2} . \tag{2.32}$$

In this case, the electronic energies have values of $\pm 3t, \pm t$ and 0, respectively, at

9) The bonding and antibonding assignment is not strictly correct for graphene because of the hexagonal symmetry.

the high symmetry points, Γ, M and K in the Brillouin zone, and the band width is $6t$, which is consistent with the three π bonds per atom.

It should be noted that the valence and conduction bands come into the K (K') point with a linear $E(k)$ relation. The $E(k)$ relation about the K and K' points was already shown to have a linear dependence of $E(k)$ in the early work of Wallace [53]. Most of the graphene literature makes use of the relation Eq. (2.32) for $s = 0$, and uses the lowest order term in the expansion of this equation around the K and K' points in the Brillouin zone, which are related by time inversion symmetry. This yields

$$E^{\pm}(k) = \pm\hbar v_{\mathrm{F}}|k| \,, \tag{2.33}$$

where v_{F} is the Fermi velocity of π electrons ($\sim 10^6$ km/s) given by

$$v_{\mathrm{F}} = \sqrt{3}(\gamma_0 a/2\hbar) \,, \tag{2.34}$$

and $a = \sqrt{3}a_{\mathrm{C\text{–}C}}$ is the lattice constant of graphene and $a_{\mathrm{C\text{–}C}} = 1.42$ Å is the nearest neighbor carbon–carbon distance [53].

It is interesting to point out that the linear dispersion given by Eq. (2.33) is the solution to the massless Dirac Hamiltonian at the $K(K')$ point [97]:

$$\mathcal{H} = \hbar v_F(\sigma \cdot \kappa) \,, \tag{2.35}$$

where $\kappa = -i\nabla$, and the σ are the Pauli matrices operating in the space of the electron wave function amplitude on the A,B sublattices of graphene (pseudo spin). Equation (2.35) gives a "chiral" nature to the quasi-particles defined by Eq. (2.33) [52]. The Dirac Hamiltonian of Eq. (2.35) (or the effective mass approximation model) gives good insights into the relativistic nature of electrons in monolayer graphene, and has been important for describing transport effects near the Fermi level. However, its accuracy is limited to low energies and care should be taken when using this expression to analyze optical phenomena. Nevertheless, in the visible range the linear k dispersion relation (see Figure 2.7) is usually accurate enough to explain most experimental results.

2.2.3 The σ-Bands of Graphene

Let us next consider the σ-bands of graphene. There are three atomic orbitals of sp^2 covalent bonding per carbon atom, $2s, 2p_x$ and $2p_y$. We thus have six Bloch orbitals in the 2 atom unit cells, yielding six σ-bands for the 6×6 Hamiltonian matrix. We calculate the electronic structure for these six σ-bands using this 6×6 Hamiltonian and the corresponding (6×6) overlap matrix, and we then solve the secular equation for each $\boldsymbol{k}$ point. Since the planar geometry of graphene satisfies the even symmetry of the Hamiltonian $\mathcal{H}$ and of the symmetry operators $2s, 2p_x$ and $2p_y$ upon mirror reflection about the xy plane, and the odd symmetry of the operator $2p_z$, the σ and π energy bands can be solved separately, because the matrix elements of different symmetry types do not couple in the Hamiltonian. For

the eigenvalues thus obtained, three of the six σ-bands are bonding σ-bands which appear below the Fermi energy, and the other three σ-bands are antibonding σ^*-bands which appear above the Fermi energy.

The calculation of the Hamiltonian and overlap matrix is performed analytically, using a small number of parameters. Hereafter we arrange the matrix elements in accordance with their atomic identity for the free atom: $2s^{\mathrm{A}}, 2p_x^{\mathrm{A}}, 2p_y^{\mathrm{A}}, 2s^{\mathrm{B}}, 2p_x^{\mathrm{B}}, 2p_y^{\mathrm{B}}$. Then the matrix elements coupling the same atoms (for example A and A) can be expressed by a 3×3 small matrix, which is a sub-matrix of the 6×6 matrix. Within the nearest neighbor site approximation, the small Hamiltonian and overlap matrices are diagonal matrices as follows:

$$\mathcal{H}_{AA} = \begin{pmatrix} \epsilon_{2s} & 0 & 0 \\ 0 & \epsilon_{2p} & 0 \\ 0 & 0 & \epsilon_{2p} \end{pmatrix}, \quad \mathcal{S}_{AA} = \begin{pmatrix} 1 & 0 & 0 \\ 0 & 1 & 0 \\ 0 & 0 & 1 \end{pmatrix}, \tag{2.36}$$

where ϵ_{2s} and ϵ_{2p} denote the orbital energy of the $2s$ and $2p$ levels.

The matrix element for the Bloch orbitals between the A and B atoms can be obtained by taking the components of $2p_x$ and $2p_y$ in the directions parallel or perpendicular to the σ bond. In Figure 2.8, we show how to rotate the $2p_x$ atomic orbital and how to obtain the σ and π components for the rightmost bonds of this figure.[10] In Figure 2.8 the wavefunction of $|2p_x\rangle$ is decomposed into its σ and π components as follows:

$$|2p_x\rangle = \cos\frac{\pi}{3}|2p_\sigma\rangle + \sin\frac{\pi}{3}|2p_\pi\rangle\ . \tag{2.37}$$

This type of decomposition is called the Slater–Koster method [94].

By rotating the $2p_x$ and $2p_y$ orbitals in the directions parallel and perpendicular to the desired bonds, the matrix elements appear in only 8 patterns as shown in Figure 2.9, where shaded and nonshaded regions denote positive and negative

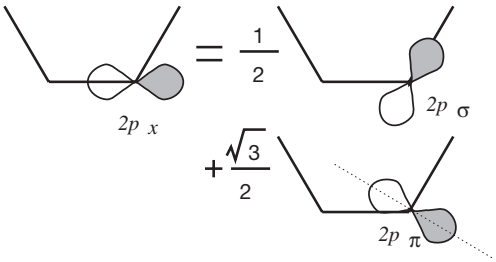

Figure 2.8 The rotation of $2p_x$. The figure shows how to project $2p_x$ into its σ and π components in the direction of the right C–C bond. This method is valid only for p orbitals [31].

10) Here the π component (in-plane) has nothing to do with the π orbital (out-of-plane) discussed in Section 2.2.2. The π component is named π because it is perpendicular to the considered σ orbital.

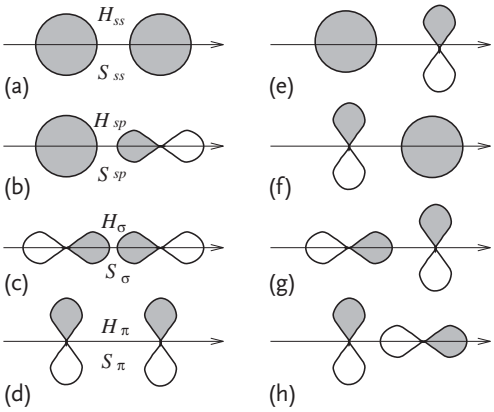

Figure 2.9 The band parameters for σ-bands. The four cases from (a) to (d) correspond to matrix elements having nonvanishing values and the remaining four cases from (e) to (h) correspond to matrix elements with zero values [31].

amplitudes of the wavefunctions, respectively. The four cases from Figure 2.9a to d correspond to nonvanishing matrix elements and the remaining four cases from Figure 2.9e to h correspond to matrix elements that vanish because of symmetry. The corresponding parameters for both the Hamiltonian and the overlap matrix elements are also shown in Figure 2.9.

When all the matrix elements of the 6×6 Hamiltonian and overlap matrices are calculated [31, 96], the energy dispersion of the σ-bands can be obtained from solution of the secular equation. Since the analytic solution of the 6×6 Hamiltonian is too complicated for practical use, we solve the Hamiltonian numerically by using, for example, the Lapack software package.[11] The results thus obtained for the calculated σ and π energy bands are shown in Figure 2.10, which result from a fit of the functional form of the energy bands imposed by symmetry to the energy values obtained from the first principles band calculations at the high symmetry points [31, 96].

2.2.4
N-Layer Graphene Systems

When joining graphene layers to form N-layer graphene (N-LG) with the Bernal AB stacking structure, the unit cell will be formed by $2N$ atoms. Consequently, the π and π^*-bands will split into symmetric and antisymmetric combinations of the graphene states. Figure 2.11a,b shows the unit cell for $N = 2$, that is, bilayer graphene (2-LG), and Figure 2.11c shows its π-band electronic structure. For 3-LG

11) Lapack is a linear algebra package written using Fortran or C languages. You can download the library as free software and the programs have been used and checked to be correct by many groups. We do not need to use a sub-program for matrix calculations but just call this library. For further details, search for "LAPACK" on the Internet. There are several versions of the Lapack library. The Intel compiler supports Lapack under the name of Math Kernel Library.

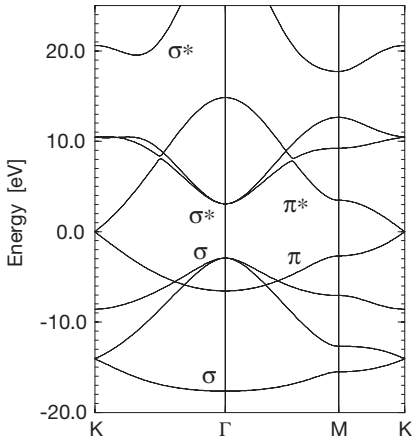

Figure 2.10 The energy dispersion relations along high symmetry directions for σ and π-bands of monolayer graphene [31]. The Fermi level (E_F) was chosen as the zero energy.

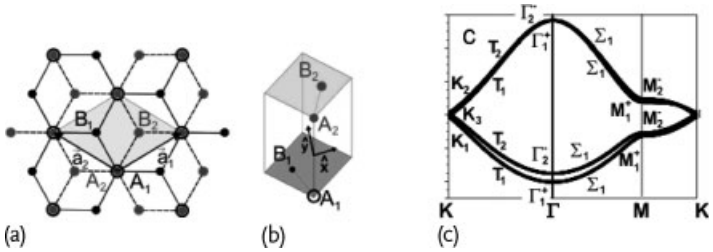

Figure 2.11 (a) The real space top-view of the setting for the unit cell for bilayer graphene (2-LG) with AB Bernal stacking, showing the non-equivalent A_1 and B_1 carbon atoms in the first layer and the A_2 and B_2 carbon atoms in the second layer. The unit cell vectors $\boldsymbol{a}_1$ and $\boldsymbol{a}_2$ are shown, considering the origin to be half way between atoms A_1 and A_2. The A atoms are above one another on adjacent layers, but the B atoms are staggered on adjacent layers, as shown in a 3D view in panel (b). (c) The electronic dispersion for the 2-LG π electrons calculated by DFT (density functional theory) along the KΓMK directions. The energy band labeling comes from group theory and will be discussed in Chapter 6 [98].

with AB stacking, atoms A_3 and B_3 would be placed on top of A_1 and B_1 in the top-view of Figure 2.11a and it would exhibit 3π and $3\pi^*$-bands. The stacking of 4-LG would look exactly like two 2-LG blocks on top of each other, and so on. The electronic structure of 2-LG can be described by the phenomenological Slonczewski–Weiss–McClure (SWM) model [16, 99, 100]. Since the unit cell of 2-LG with the Bernal AB stacking structure is the same as for graphite, which also has the same layer stacking structure, we can denote the electronic spectrum of bilayer graphene in terms of a model closely related to the SWM model for graphite. A larger set of parameters (γ_0, γ_1, γ_3, and γ_4),[12)] that are associated with overlap and transfer integrals calculated for nearest neighbors atoms up to adjacent layers will be need-

12) γ_2 and γ_5 are transfer integrals for next-nearest layers.

ed to describe the electronic structure (more about this in Section 11.3). However, even in 3D graphite, the interaction between two adjacent layers is small compared with intralayer interactions, since the layer-layer separation of 3.35 Å is much larger than the nearest neighbor distance between two carbon atoms, $a_{C\text{–}C} = 1.42$ Å. Thus the electronic structure of graphene provides a building block for the electronic structure for N-LG and 3D graphite.

One important fact for N-LG is that the linear energy dispersion of 1-LG appears for odd-number LG near the Fermi energy, while parabolic energy dispersion appears for even-number LG. Koshino and Ando [101] explain this fact by showing that the Hamiltonian can be decoupled into 2×2 sub-matrices if we consider only γ_1 for the interlayer interaction [101]. Thus depending on whether we have an odd or even number of graphene layers, the effective mass of the carriers of N-LG becomes zero or finite, respectively, which is analogous to elementary particle physics in which two kinds of particles exist, such as massless (photon, neutrino) Bosons, and finite mass (electron, proton) Fermions depending on symmetry. When we consider the Fermi velocity $v_F = 1 \times 10^6$ m/s, which is $\sim c/300$ as the velocity of light, we can make an analogy between graphene and particle physics.

2.2.5 Nanoribbon Structure

When going from a bulk material to a low-dimensional structure, the electronic states are constrained by quantum effects in the nanoscale directions. If the low-dimensional system has the same crystal structure as the parent higher-dimensional material, the electronic states of the low-dimensional system can be considered as a subset of the electronic states of the bulk material. When we move from the two-dimensional graphene sheet to the one-dimensional carbon nanoribbon (or nanotube), the wave vector components in the nanoscale directions can only take on discrete values in order to maintain an integral number of wave function nodes, that is, these wave vector components then become quantized. The number of quantized states for a given orbital of each atom (such as $2s, 2p_x \ldots$) is equal to the number of unit cells of the parent higher-dimensional material in the nanoscale directions of the lower-dimensional structure.

The general procedure for confining the two-dimensional electronic structure of graphene into a one-dimensional structure will be discussed in detail for carbon nanotubes in Section 2.3. But before discussing nanotubes in detail, let us briefly mention graphene nanoribbons. Such nanoribbons consist of graphene with a finite width and infinite length, as shown in Figure 2.12. Thus the unit cell of a nanoribbon consists of 2N carbon atoms[13] in the direction of the width, while periodicity appears in the length direction. The wavevectors are quantized in the direction of the width, and 2N 1D energy sub-bands for the π ($2p_z$) band appears if we simply adopt the zone-folding method (see Figure 2.13).

13) Here N is the number of CC dimers along the ribbon width. Here we use *N* (italic font) for the number of graphene layers.

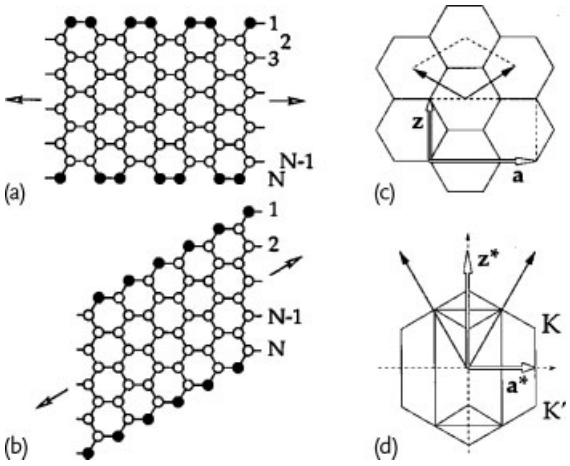

Figure 2.12 (a,b) The network skeleton of two nanoribbons. (a) N = 10 lines of C atoms from one edge to the other, and an armchair-like edge structure. (b) N = 5 and a zigzag-like edge structure. The arrows indicate the translational directions of the graphene ribbons. Unit cells in real space (c) and reciprocal space (d) of 2D graphite. The vectors $\boldsymbol{a}$ and $\boldsymbol{a}^*$ (z and z^*) relate to armchair (zigzag) ribbons [102].

The method of constructing 1D electronic energy sub-bands by *cutting* the 2D electronic dispersion relations with these lines is known as the "zone-folding scheme" [31]. The cutting lines represent the allowed k vectors for the 1D nanorib-

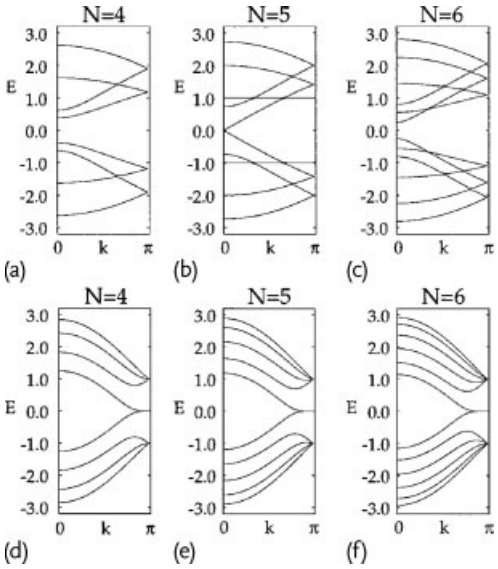

Figure 2.13 Band structure $E(k)$ of graphene nanoribbons of various widths obtained from the zone-folding procedure. Armchair nanoribbons with N = 4 (a), N = 5 (b) and N = 6 (c), and zigzag nanoribbons with N = 4 (d), N = 5 (e), and N = 6 (f) [102].

bon represented in the 2D Brillouin zone of graphene, which are continuous along the ribbon axis and discrete along the tube width. The length of each cutting line is $2\pi/T$, where T is the 1D unit vector in the translational direction of the nanoribbon or nanotube axis. The separation between two adjacent cutting lines is inversely proportional to the nanoribbon width (nanotube diameter). The orientation of the cutting lines in 2D reciprocal space is determined by the cutting direction, that is, the relative orientation of the nanoribbon axis with respect to the principal axes of graphene (the unrolled flat layer of the 2D parent graphene material [31]). The structure of the edges is very important. We can consider two possible edges, armchair and zigzag edges, which are more stable than the other shape of edges [103] and whose structures are shown in Figure 2.12. The nanoribbons with armchair and zigzag edges are called, respectively, armchair nanoribbons (A-NR) and zigzag nanoribbons (Z-NR). For both cases, the edge carbon atoms have two σ bonds and one π bond, while the remaining σ bonds exist as either being terminated by H atoms or by dangling bonds.

We see that for the π-band for nanoribbons, a flat energy band appears around the Fermi energy in the electronic energy dispersion from the K to M points for Z-NRs (see Figure 2.13d–f), while no edge states appear for A-NRs (see Figure 2.13a–c). Thus the density of states near the Fermi energy is singular for Z-NRs. In the case of A-NRs, the energy gap is oscillating as a function of N, and for $N = 3n - 1$ the A-NRs become metallic, while they are semiconducting in the other cases (see Figure 2.13a–c).

While the zone-folding procedure works as a first approximation to the electronic structure for nanoribbons, the presence of edge states can significantly alter their fundamental electronic properties. For example, different from what is shown in Figure 2.13, *ab initio* calculations [104] and experiments [105] show that because of the localized edge states, all nanoribbons are semiconducting materials with an energy gap magnitude depending on the ribbon width, which depends on N. The electron amplitude ratio between sites A and B is expressed by the pseudo-spin, and the edge states in Z-NRs can be understood as pseudo-spin polarized states. From this we can derive many interesting physical phenomena, such as half-metallicity (only one of two spin currents exist at the Fermi energy) and the occurrence of magnetism at the zigzag edges [104, 106]. Once you close the ribbon structure into a carbon nanotubes, this complex edge physics is gone, as discussed in the next section.

2.3
Electrons in Single-Wall Carbon Nanotubes

In this section we review the structure of carbon nanotubes (Section 2.3.1), their electronic dispersion relations (Section 2.3.2), and their density of electronic states (Section 2.3.3). In Section 2.3.4 we explain the importance of both the carbon nanotube electronic structure and the laser excitation energy on the details of the observed Raman spectra.

2.3.1
Nanotube Structure

A single-wall carbon nanotube (SWNT) is constructed starting from a graphene layer by rolling it up into a seamless cylinder [31]. The graphene layer is oriented with respect to the coordinate system in such a way that the armchair direction lies along the x-axis and the zigzag direction is along the y-axis, as shown in Figure 2.14. The nanotube structure is uniquely determined by the chiral vector $\boldsymbol{C}_h$ which spans the circumference of the cylinder when the graphene layer is rolled up into a tube. The chiral vector can be written in the form $\boldsymbol{C}_h = n\boldsymbol{a}_1 + m\boldsymbol{a}_2$, where n and m are integers and where the vectors $\boldsymbol{a}_1$ and $\boldsymbol{a}_2$ bounding the unit cell of the graphene layer with the two distinct carbon atom sites A and B are shown in Figure 2.14. In the shortened (n, m) form, the chiral vector is written as a pair of integers, and the same notation is widely used to characterize the geometry of each distinct (n, m) nanotube.

The nanotube can also be characterized by its diameter d_t and chiral angle θ from a zigzag direction, which determine the length $C_h = |\boldsymbol{C}_h| = \pi d_t$ of the chiral vector and its orientation on the graphene layer (see Figure 2.14). Both d_t and θ are expressed in terms of the indices n and m by the relations $d_t = a\sqrt{n^2 + nm + m^2}/\pi$ and $\tan\theta = \sqrt{3}m/(2n + m)$, as one can derive from Figure 2.14, where $a = |\boldsymbol{a}_1| = |\boldsymbol{a}_2| = \sqrt{3}a_{C\text{–}C} = 0.246\,\text{nm}$ is the lattice constant for the graphene layer and $a_{C\text{–}C} = 0.142\,\text{nm}$ is the nearest neighbor C–C distance [31]. As an example, the chiral vector $\boldsymbol{C}_h$ shown in Figure 2.14 is given by $\boldsymbol{C}_h = 4\boldsymbol{a}_1 + 2\boldsymbol{a}_2$, and thus the corresponding nanotube can be identified by the integer pair (4, 2). Due to the six-fold symmetry of one graphene layer, all non-equivalent nanotubes can be characterized by the (n, m) pairs of integers where

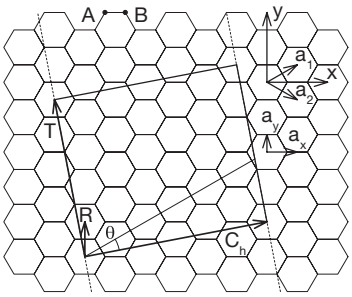

Figure 2.14 An unrolled nanotube projected on the graphene layer. When the nanotube is rolled up, the chiral vector $\boldsymbol{C}_h$ turns into the circumference of the cylinder, and the translation vector $\boldsymbol{T}$ is aligned along the cylinder axis. $\boldsymbol{R}$ is the symmetry vector and θ is the chiral angle (see text). The unit vectors $(\boldsymbol{a}_1, \boldsymbol{a}_2)$ of the graphene layer are indicated.[14] The non-equivalent A and B sites within the unit cell of the graphene layer are shown at the top [31].

14) Notice the origin of the $(\boldsymbol{a}_1, \boldsymbol{a}_2)$ in this figure are chosen differently from that described in Figure 2.6a.

$0 \le m \le n$. The nanotubes are classified as chiral ($0 < m < n$) and achiral ($m = 0$ or $m = n$), which in turn are known as zigzag ($m = 0$) and armchair ($m = n$) nanotubes. A (4, 2) chiral nanotube is one of the smallest diameter nanotubes ever synthesized [107], requiring special calculational treatment because of its large curvature [108].

The unit cell of an unrolled nanotube on a graphene layer is a rectangle bounded by the vectors $\boldsymbol{C}_h$ and translational vector $\boldsymbol{T}$ (see the rectangle shown in Figure 2.14 for the (4, 2) nanotube). $\boldsymbol{T}$ is given by $t_1\boldsymbol{a}_1 + t_2\boldsymbol{a}_2$, where integers t_1 and t_2 are obtained by $\boldsymbol{C}_h \cdot \boldsymbol{T} = 0$ and $\mathrm{gcm}(t_1, t_2) = 1$. Here gcm is an integer function of the greatest common multiplier of (n, m). The area of the nanotube unit cell can be easily calculated as a vector-product of these two vectors, $|\boldsymbol{C}_h \times \boldsymbol{T}| = \sqrt{3}a^2\left(n^2 + nm + m^2\right)/d_R$, where $d_R = \mathrm{gcm}(2n + m, 2m + n)$. Using d_R, then t_1 and t_2 are given by $t_1 = (2m + n)/d_R$ and $t_2 = -(2n + m)/d_R$.

Dividing the cross product $|\boldsymbol{C}_h \times \boldsymbol{T}|$ by the area of the unit cell of a graphene layer $|\boldsymbol{a}_1 \times \boldsymbol{a}_2| = \sqrt{3}a^2/2$, one can get the number of hexagons in the unit cell of a nanotube, $N = 2\left(n^2 + nm + m^2\right)/d_R$. For the (4, 2) nanotube we have $N = 28$, so that the unit cell of the (4, 2) nanotube (see the rectangle shown in Figure 2.14) contains 28 hexagons, or $2 \times 28 = 56$ carbon atoms (see Table 2.1) [31].

The unit cell of a graphene layer is defined by the vectors $\boldsymbol{a}_1$ and $\boldsymbol{a}_2$. The graphene reciprocal lattice unit vectors $\boldsymbol{b}_1$ and $\boldsymbol{b}_2$ can be constructed from $\boldsymbol{a}_1$ and $\boldsymbol{a}_2$ using the standard definition $\boldsymbol{a}_i \cdot \boldsymbol{b}_j = 2\pi\delta_{ij}$, where δ_{ij} is the Kronecker delta symbol. The resulting reciprocal lattice unit vectors, $\boldsymbol{b}_1 = \boldsymbol{b}_x + \boldsymbol{b}_y$ and $\boldsymbol{b}_2 = \boldsymbol{b}_x - \boldsymbol{b}_y$, where $\boldsymbol{b}_x = 2\pi\hat{\boldsymbol{k}}_x/\left(\sqrt{3}a\right)$ and $\boldsymbol{b}_y = 2\pi\hat{\boldsymbol{k}}_y/a$, form the unit vectors for the hexagonal reciprocal lattice, as shown in Figure 2.15. Note the rotation of the hexagons in real space (Figure 2.14) and in reciprocal space (Figure 2.15).

In a similar fashion, the reciprocal space of a nanotube can be constructed [31]. The unrolled unit cell of the nanotube on a graphene layer is defined by the vectors $\boldsymbol{C}_h$ and $\boldsymbol{T}$, and therefore the reciprocal space vectors for the nanotube, $\boldsymbol{K}_1$ and $\boldsymbol{K}_2$, can be constructed using the standard definition, $\boldsymbol{C}_h \cdot \boldsymbol{K}_1 = \boldsymbol{T} \cdot \boldsymbol{K}_2 = 2\pi$ and $\boldsymbol{C}_h \cdot \boldsymbol{K}_2 = \boldsymbol{T} \cdot \boldsymbol{K}_1 = 0$. The vector $\boldsymbol{K}_1$ can be written in the form $\boldsymbol{K}_1 \propto t_2\boldsymbol{b}_1 - t_1\boldsymbol{b}_2$ to provide its orthogonality to the vector $\boldsymbol{T}$, taking into account that $\boldsymbol{a}_i \cdot \boldsymbol{b}_j = 2\pi\delta_{ij}$. Similarly, $\boldsymbol{K}_2 \propto m\boldsymbol{b}_1 - n\boldsymbol{b}_2$ is orthogonal to $\boldsymbol{C}_h$. The normalization conditions

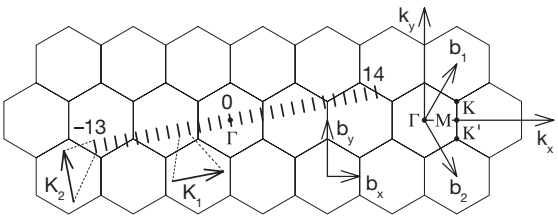

Figure 2.15 Reciprocal space of the graphene layer. Parallel equidistant lines represent the cutting lines for the (4, 2) nanotube, labeled by the cutting line index μ, which assumes values from $1 - N/2 = -13$ to $N/2 = 14$. The reciprocal lattice unit vectors $(\boldsymbol{b}_1, \boldsymbol{b}_2)$ are indicated in this figure along with the (zoomed) reciprocal lattice unit vectors $(\boldsymbol{K}_1, \boldsymbol{K}_2)$ of the nanotube [31].

$\boldsymbol{C}_h \cdot \boldsymbol{K}_1 = \boldsymbol{T} \cdot \boldsymbol{K}_2 = 2\pi$ are used to calculate the proportionality coefficients, yielding the magnitudes of the reciprocal space vectors, $|\boldsymbol{K}_1| = 2/d_t$ and $|\boldsymbol{K}_2| = 2\pi/|\boldsymbol{T}|$. This results in the following expressions for the reciprocal space vectors, $\boldsymbol{K}_1 = -(t_2\boldsymbol{b}_1 - t_1\boldsymbol{b}_2)/N$ and $\boldsymbol{K}_2 = (m\boldsymbol{b}_1 - n\boldsymbol{b}_2)/N$ (see Table 2.1). Using the reciprocal space vectors $\boldsymbol{K}_1$ and $\boldsymbol{K}_2$, we can now construct the cutting lines for the nanotube as shown in Figure 2.15. The vectors $\boldsymbol{K}_1$ and $\boldsymbol{K}_2$ are orthogonal, and $\boldsymbol{K}_2$ is directed along the nanotube axis, so that the cutting lines are also aligned along the tube axis.

The unrolled nanotube is extended in the direction of the translation vector $\boldsymbol{T}$ and has a nanoscale size in the direction of the chiral vector $\boldsymbol{C}_h$ (see Figure 2.14). Since the translation vector $\boldsymbol{T}$ is collinear with the wave vector $\boldsymbol{K}_2$, and the chiral vector $\boldsymbol{C}_h$ corresponds to the wave vector $\boldsymbol{K}_1$, the unrolled reciprocal space of the nanotube (see Figure 2.15) is quantized along the $\boldsymbol{K}_1$ direction and is continuous along the $\boldsymbol{K}_2$ direction.

Consequently, the N wave vectors $\mu\boldsymbol{K}_1$, where μ is an integer number varying from $(1 - N/2)$ to $N/2$ (note that N is always even), form the N quantized states in the direction $\boldsymbol{K}_1$ of the unrolled reciprocal space of the nanotube. Each of these N quantized states gives rise to a line segment of length $K_2 = |\boldsymbol{K}_2|$ along the direction $\boldsymbol{K}_2$ in the unrolled reciprocal space of the nanotube. These N line segments, defined by the wave vectors $\boldsymbol{K}_1$ and $\boldsymbol{K}_2$, represent the cutting lines in the unrolled reciprocal space of the nanotube. The length and orientation of each cutting line in reciprocal space is given by the wave vector $\boldsymbol{K}_2$, while the separation between two adjacent cutting lines is given by the wave vector $\boldsymbol{K}_1$. In the case of our model (4, 2) nanotube, the $N = 28$ cutting lines are shown in Figure 2.15 numbered by the index μ varying from $1 - N/2 = -13$ to $N/2 = 14$, where the middle cutting line $\mu = 0$ crosses the Γ point, the center of the first Brillouin zone of the graphene layer. In the case of an ideal infinitely long nanotube, the wave vectors along the nanotube axis (along the $\boldsymbol{K}_2$ vector) would be continuous. If the nanotube length L is small enough, yet still much larger than the unit cell length $T = |\boldsymbol{T}|$, the wave vector along the nanotube axis also becomes quantized, $\xi(T/L)\boldsymbol{K}_2$, where ξ is an integer number ranging from $(2T - L)/(2T)$ to $L/(2T)$. Such quantization effects in short carbon nanotubes have been observed experimentally [109]. The SWNT parameters are summarized in Table 2.1.

2.3.2
Zone-Folding of Energy Dispersion Relations

The electronic structure of a single-wall nanotube can be obtained simply from that of two-dimensional graphite. By using periodic boundary conditions in the circumferential direction denoted by the chiral vector $\boldsymbol{C}_h$, the wave vector associated with the $\boldsymbol{C}_h$ direction becomes quantized, while the wave vector associated with the direction of the translational vector $\boldsymbol{T}$ (or along the nanotube axis) remains

Table 2.1 Parameters for single-wall carbon nanotubes.[a]

Symbol	Name	Formula
a	Graphene lattice constant	$a = \sqrt{3}a_{\mathrm{C\text{–}C}} = 0.246\,\mathrm{nm}$
$\boldsymbol{a}_1,\ \boldsymbol{a}_2$	Graphene unit vectors	$\left(\frac{\sqrt{3}}{2}, \frac{1}{2}\right)a,\ \left(\frac{\sqrt{3}}{2}, -\frac{1}{2}\right)a$
$\boldsymbol{b}_1,\ \boldsymbol{b}_2$	Graphene reciprocal lattice vectors	$\left(\frac{1}{\sqrt{3}}, 1\right)\frac{2\pi}{a},\ \left(\frac{1}{\sqrt{3}}, -1\right)\frac{2\pi}{a}$
$\boldsymbol{C}_h$	Nanotube chiral vector	$\boldsymbol{C}_h = n\boldsymbol{a}_1 + m\boldsymbol{a}_2 \equiv (n, m)$
C_h	Length of $\boldsymbol{C}_h$	$C_h = \lvert\boldsymbol{C}_h\rvert = a\sqrt{n^2 + m^2 + nm}$
d_t	Nanotube diameter	$d_t = C_h/\pi$
θ	Nanotube chiral angle	$\tan\theta = \frac{\sqrt{3}m}{2n+m}$
d	$\gcd(n, m)$[b]	
d_R	$\gcd(2n + m, 2m + n)$[b]	$d_R = \begin{cases} d & \text{if } (n-m) \text{ is not a multiple of } 3d \\ 3d & \text{if } (n-m) \text{ is a multiple of } 3d \end{cases}$
N	Number of hexagons in the nanotube unit cell	$N = \frac{2(n^2+m^2+nm)}{d_R}$
$\boldsymbol{T}$	Translational vector along nanotube axis	$\boldsymbol{T} = t_1\boldsymbol{a}_1 + t_2\boldsymbol{a}_2$
$t_1,\ t_2$		$t_1 = \frac{2m+n}{d_R},\ \ t_2 = -\frac{2n+m}{d_R}$
T	Length of $\boldsymbol{T}$	$T = \lvert\boldsymbol{T}\rvert = \frac{\sqrt{3}C_h}{d_R}$
$\boldsymbol{R}$	Symmetry vector of the nanotube	$\boldsymbol{R} = p\boldsymbol{a}_1 + q\boldsymbol{a}_2$
$p,\ q$		$t_1 q - t_2 p = 1,\ \ 1 \le mp - nq \le N$
τ	Pitch of $\boldsymbol{R}$	$\tau = \frac{(mp-nq)T}{N} = \frac{MT}{N}$
ψ	Rotation angle of $\boldsymbol{R}$	$\psi = \frac{2\pi}{N}$
M	Number of $\boldsymbol{T}$ in $N\boldsymbol{R}$	$N\boldsymbol{R} = \boldsymbol{C}_h + M\boldsymbol{T},\ \ M = mp - nq$
$\boldsymbol{K}_1$	Nanotube reciprocal lattice vectors	$\boldsymbol{K}_1 = -(t_2\boldsymbol{b}_1 - t_1\boldsymbol{b}_2)/N$
$\boldsymbol{K}_2$		$\boldsymbol{K}_2 = (m\boldsymbol{b}_1 - n\boldsymbol{b}_2)/N$
		$K_1 = \lvert\boldsymbol{K}_1\rvert = 2/d_t K_2 = \lvert\boldsymbol{K}_2\rvert = 2\pi/T$
		$\boldsymbol{K}_1 \parallel \boldsymbol{C}_h$
		$\boldsymbol{K}_2 \parallel \boldsymbol{T}$
	Translational vectors for the $\boldsymbol{K}_1$-extended representation of the cutting lines	$N\boldsymbol{K}_1 = -t_2\boldsymbol{b}_1 + t_1\boldsymbol{b}_2$
		$\boldsymbol{K}_2 - M\boldsymbol{K}_1 = \frac{m+Mt_2}{N}\boldsymbol{b}_1 - \frac{n+Mt_1}{N}\boldsymbol{b}_2$
	Translational vectors for the $\boldsymbol{K}_2$-extended representation of the cutting lines	$(N/Q)\boldsymbol{K}_2 = \frac{m}{Q}\boldsymbol{b}_1 - \frac{n}{Q}\boldsymbol{b}_2$
		$Q\boldsymbol{K}_1 - W\boldsymbol{K}_2 = r_1\boldsymbol{b}_1 + r_2\boldsymbol{b}_2$
Q		$Q = \gcd(M, N)$[b]
W		$W = r_2 t_2 - r_1 t_1$
$r_1,\ r_2$		$nr_1 - mr_2 = Q,\ \ 1 \le t_2 r_2 - t_1 r_1 \le \frac{N}{Q}$

a In this table $n, m, t_1, t_2, r_1, r_2, p$, and q are integers and d, d_R, N, M, Q, and W are integer functions of these integers.

b $\gcd(n, m)$ denotes the greatest common divisor of the two integers n and m.

continuous for a nanotube of infinite length.[15] Figure 2.16 shows the reciprocal space of the (4,2) nanotube ($\boldsymbol{\kappa}_1 = 28\boldsymbol{K}_1$ and $\boldsymbol{\kappa}_2 = \boldsymbol{K}_2 - 6\boldsymbol{K}_1$) as compared to the graphene reciprocal space. The first Brillouin zone, which is shown in dark gray, can be translated to the adjacent Brillouin zones, shown in light gray, by applying reciprocal lattice vectors, as shown in Figure 2.16. Thus the energy bands consist of a set of one-dimensional energy dispersion relations which are cross-sections of those for two-dimensional graphite (see Figure 2.17a).

When the energy dispersion relations of two-dimensional graphite are folded, N pairs of 1D energy dispersion relations $E_\mu(k)$ are obtained (see Figure 2.17b).

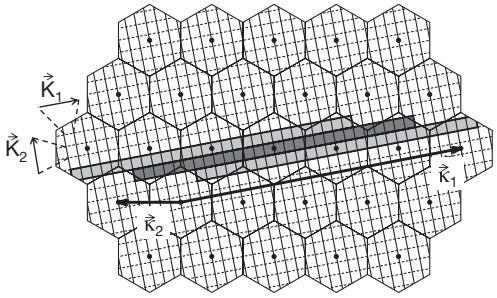

Figure 2.16 Reciprocal space of the graphene layer, showing the $\boldsymbol{K}_1$ and $\boldsymbol{K}_2$ reciprocal lattice vectors. Parallel equidistant lines represent the cutting lines for the (4, 2) nanotube. The first Brillouin zone is shown in dark gray. The light gray rectangles are the Brillouin zones obtained by the unit vector $\boldsymbol{\kappa}_2$ of the reciprocal space structures [110].

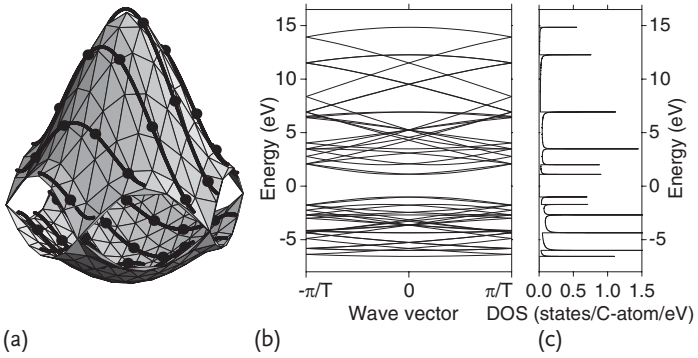

Figure 2.17 (a) The conduction and valence bands of the graphene layer in the first Brillouin zone calculated according to the π-band nearest neighbor tight-binding model [31]. Solid curves show the cutting lines for the (4, 2) nanotube in the fully reduced representation. Solid dots show the ends of the cutting lines in the fully $\boldsymbol{K}_1$-extended representation. (b) Electronic energy band diagram for the (4, 2) nanotube obtained by zone-folding from (a). (c) Density of electronic states for the energy band diagram shown in (b) [110].

15) For real carbon nanotubes, if the length of a nanotube (L_{CN}) is on the order of a micrometer or less, discrete k vectors ($\Delta k = 2\pi/L_{CN}$) can be expected.

These 1D energy dispersion relations are given by

$$E_\mu(k) = E_{g2D}\left(k\frac{\boldsymbol{K}_2}{|\boldsymbol{K}_2|} + \mu\boldsymbol{K}_1\right), \quad \left(\mu = 0, \cdots, N-1, \quad \text{and} \quad -\frac{\pi}{T} < k < \frac{\pi}{T}\right), \tag{2.38}$$

corresponding to the energy dispersion relations of a single-wall carbon nanotube, where E_{g2D} comes from Eq. (2.30). The N pairs of energy dispersion curves given by Eq. (2.38) correspond to the cross-sections of the two-dimensional energy dispersion surface shown in Figure 2.17a, where cuts are made on the lines of $k\boldsymbol{K}_2/|\boldsymbol{K}_2| + \mu\boldsymbol{K}_1$.

If for a particular (n, m) nanotube, a cutting line passes through a K point of the 2D Brillouin zone, where the π and π^* energy bands of two-dimensional graphite are degenerate by symmetry, then the one-dimensional energy bands have a zero energy gap, and are metallic. If, however, no cutting line passes through a K point, then the carbon nanotube is expected to show semiconducting behavior, with a finite energy gap between the valence and conduction bands.

The condition for obtaining a metallic energy band is that the ratio of the length of the vector $\boldsymbol{YK}$ to that of $\boldsymbol{K}_1$ in Figure 2.18 is an integer.[16] Since the vector $\boldsymbol{YK}$ is given by

$$\boldsymbol{YK} = \frac{2n+m}{3}\boldsymbol{K}_1\,, \tag{2.39}$$

the condition for metallic nanotubes is that $(2n + m)$ or equivalently $(n - m)$ is a multiple of 3.[17] In particular, the armchair nanotubes denoted by (n, n) are always

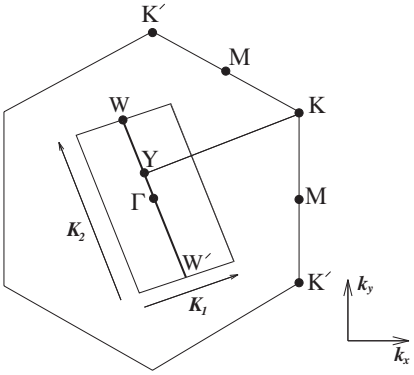

Figure 2.18 The condition for metallic energy bands: if the ratio of the length of the vector $\boldsymbol{YK}$ to that of $\boldsymbol{K}_1$ is an integer, metallic energy bands are obtained [31].

16) There are two non-equivalent K and K' points in the Brillouin zone of graphite as is shown in Figure 2.18 and thus the metallic condition can also be obtained in terms of K'. However, the results in that case are identical to the case specified by YK in Figure 2.18, since K and K' are a time-reversal pair in the k space.

17) Since $3n$ is a multiple of 3, the two remainders of $(2n + m)/3$ and $(n - m)/3$ are identical.

metallic, and the zigzag nanotubes $(n, 0)$ are only metallic when n is a multiple of 3.

The cutting lines in the vicinity of the K point are shown in Figure 2.19 for three different cases, $n - m = 3\ell$, $n - m = 3\ell + 1$, and $n - m = 3\ell + 2$, where ℓ is an integer. The first case $n - m = 3\ell$ corresponds to the cutting line crossing the K point, resulting in metallic behavior, as discussed above. The other two cases $n - m = 3\ell+1$ and $n-m = 3\ell+2$ (or, equivalently, $2n+m = 3\ell+2$ and $2n+m = 3\ell+1$, respectively, using a different notation) correspond to the K point being located at one third and at two thirds of the distance between two adjacent cutting lines, resulting in semiconducting behavior, since the cutting lines do not go through the K and K' points. We thus conclude that the number of semiconducting nanotubes is roughly twice that of metallic nanotubes.

The two cases of semiconducting nanotubes, $n-m = 3\ell+1$ and $n-m = 3\ell+2$, are also different from each other, depending on which side of the K point in the unfolded two-dimensional Brillouin zone of the nanotube the first van Hove singularity (vHS) in the electronic density of states (DOS) appears, as discussed further in Section 2.3.3. We classify these two types of semiconducting nanotubes as mod1 and mod2, in accordance with the number $(n - m - 3\ell)$ being equal to either 1 or 2, respectively. In the other notation, for $2n + m = 3\ell + 1$ and $2n + m = 3\ell + 2$, we call respectively, type I and type II (or S1 and S2). We must be careful for different notations used in the literature [110] where mod 1 (mod 2) corresponds to S2 (S1). In a similar fashion, we can classify metallic nanotubes by the ratio that the K point divides the cutting line in the $\boldsymbol{K}_1$-extended representation.

2.3.3
Density of States

As shown in the previous section, when 1D nanotubes are rolled up from 2D sheets of graphene, different sub-bands in the 1D reciprocal space of the nanotube can be

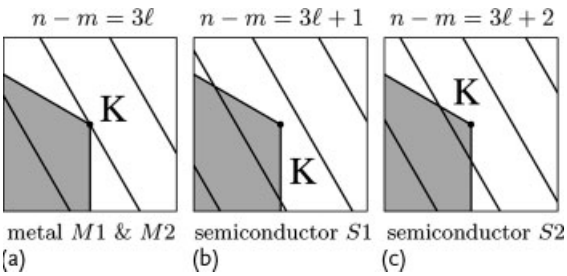

Figure 2.19 Three different configurations of the cutting lines in the vicinity of the K point. (a) Configuration $n - m = 3\ell$ corresponds to the case of metallic nanotubes of both $M1$ and $M2$ types. (b, c) Configurations $n - m = 3\ell + 1$ and $n - m = 3\ell + 2$ correspond to the case of semiconducting nanotubes of types mod 1 (or type 2 $S2$) and mod 2 (or type 1 $S1$), respectively [110].

extended into the 2D reciprocal space of a single sheet of the parent bulk layered material as a set of parallel equidistant lines or cutting lines. This procedure is shown in Figure 2.20a for states near the *K* point.

Figure 2.20b shows the electronic density of states (DOS) related to the nanotube electronic band structure plotted schematically in Figure 2.20a (see also Figure 2.17c). Each of the cutting lines in Figure 2.20a (except for the one that crosses the degenerate *K* point) gives rise to a local maximum in the DOS in Figure 2.20b, known as a (one-dimensional) van Hove singularity (vHS), given by

$$g(E) = \frac{2}{N}\sum_{\mu=1}^{N}\int\left[\frac{\partial E_\mu(k)}{\partial k}\right]^{-1}\delta[E_\mu(k) - E]dk\ . \tag{2.40}$$

The four vHS in Figure 2.20b are labeled by $E_i^{(v)}$ and $E_i^{(c)}$ for the electronic sub-bands in the valence and conduction bands, correspondingly. The presence of vHSs in the DOS of 1D structures makes these structures behave differently from their related 3D and 2D materials, as can be seen in Figure 2.21.

More generally, the DOS profiles for systems of different dimensionality (3D, 2D, 1D, and 0D) are very different from one another, as shown in Figure 2.21. The typical DOS dependence on energy near an energy band extremum, $g(E)$ is given by $g \propto (E - E_0)^{[(D/2)-1]}$, where D is an integer, denoting the spatial dimension and D

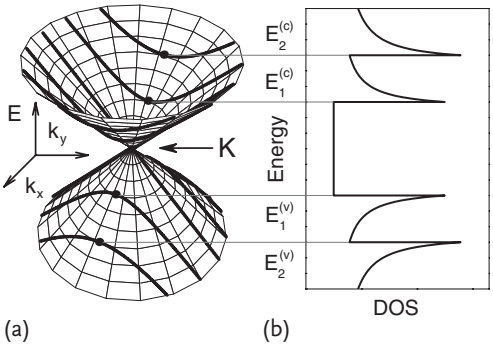

Figure 2.20 (a) The energy-momentum contours for the valence and conduction bands for a 2D system, each band obeying a linear dependence for $E(k)$ and forming a degenerate point *K* where the two bands touch to define a zero gap semiconductor. The cutting lines of these contours denote the dispersion relations for the 1D system derived from the 2D system. Each cutting line gives rise to a different energy sub-band. The energy extremum E_i for each cutting line at the wave vector k_i is known as the van Hove singularity. The energies $E_i^{(v)}$ and $E_i^{(c)}$ for the valence and conduction bands and the corresponding wave vectors $k_i^{(v)}$ and $k_i^{(c)}$ at the van Hove singularities are indicated on the figure by the solid dots. (b) The 1D density of states (DOS) for the conduction and valence bands in (b) corresponding to the $E(k)$ dispersion relations for the sub-bands shown in (a) as thick curves. The DOS shown in (b) is for a metallic 1D system, because one of the cutting lines in (a) crosses the degenerate Dirac point (the *K* point in the graphite Brillouin zone). For a semiconducting 1D system, no cutting line crosses the degenerate point, which results in a band gap opening up in the DOS between the van Hove singularities $E_1^{(v)}$ and $E_1^{(c)}$ [110].

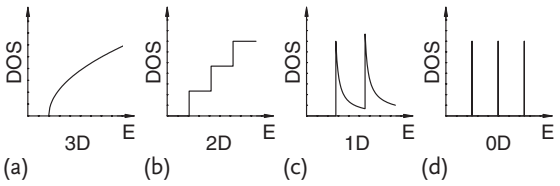

Figure 2.21 Typical electronic density of states for (a) 3D, (b) 2D, (c) 1D and (d) 0D systems [90].

assumes the values 1,2, and 3, respectively, for 1D, 2D, and 3D systems [90]. Here E_0 denotes the energy band minimum (or maximum) for the conduction (valence) energy bands. For a 1D system, E_0 would correspond to a vHS in the DOS occurring at each sub-band edge, where the magnitude of the DOS becomes very large. One can see from Figure 2.21 that 1D systems exhibit DOS profiles, which are quite similar to the case of 0D systems, with both 0D and 1D systems having very sharp maxima at certain energies, in contrast to the DOS profiles for 2D and 3D systems, which show a more monotonic increase with energy (see Figure 2.21). However, the 1D DOS is different from the 0D DOS (δ function at energy levels) in that the 1D DOS has a sharp threshold and a decaying tail, so that the 1D DOS does not go to zero between the sharp maxima, as the 0D DOS does (see Figure 2.21). The extremely high values of the DOS at the vHS allow us to observe physical phenomena for individual 1D objects in various experiments, as discussed in Section 2.3.4.

For metallic nanotubes, a cutting line crosses the Fermi level at the K point. It follows that the density of states per unit length along the nanotube axis is a constant given by

$$N(E_F) = \frac{8}{\sqrt{3}\pi a|t|} , \tag{2.41}$$

where a is the lattice constant of the graphene layer and $|t|$ is the nearest neighbor C–C tight-binding overlap energy usually denoted by γ_0 in the graphite literature [111].

For semiconducting nanotubes the DOS is zero up to the first van Hove singularities, and their energy gap depends roughly on $1/d_t$, the reciprocal nanotube diameter d_t[18)]

$$E_g = \frac{|t|a_{C\text{–}C}}{d_t} , \tag{2.42}$$

where $a_{C\text{–}C} = a/\sqrt{3}$ is the nearest neighbor C–C distance on a graphene sheet.

18) The energy gap also has a weak dependence on the chiral angle of the semiconducting nanotube.

2.3.4
Importance of the Electronic Structure and Excitation Laser Energy to the Raman Spectra of SWNTs

Figure 2.22a–c shows the density of electronic states (DOS) for three different SWNTs, and since SWNTs are one-dimensional (1D) systems, their DOS is characterized by their van Hove singularities (vHSs). The sharp vHSs define narrow energy ranges where the DOS intensity becomes very large. Therefore, in practice, a single carbon nanotube exhibits a "molecular-like" behavior, with well-defined electronic energy levels at each vHS. The three DOS curves in Figure 2.22a–c come from different SWNTs as labeled by their (n, m) indices [112] (see figure caption). An observable Raman signal from a carbon nanotube can be obtained when the laser excitation energy is equal to the energy separation between vHSs in the valence and conduction bands (e. g., see E_{11}^S, E_{22}^S and E_{11}^M in Figure 2.22), but restricted to the selection rules for optically allowed electronic transitions (see Chapter 6). A plot of the density of valence-conduction states fulfilling these selection rules that are available for optical transitions as a function of the excitation photon energy is called a joint density of states (JDOS) plot.

For the characterization of nanotubes by Raman spectroscopy, it is useful to consider plots of the energies E_{ii} vs. the nanotube diameter, d_t, as shown in Figure 2.22d [113]. Each point in this plot represents one optically allowed electronic transition energy (E_{ii}) from a given (n, m) SWNT. Crosses come from semiconducting SWNTs, and circles from metallic SWNTs. This plot should be considered as a guide for answering the question "if I use a given E_{laser} to excite my sample,

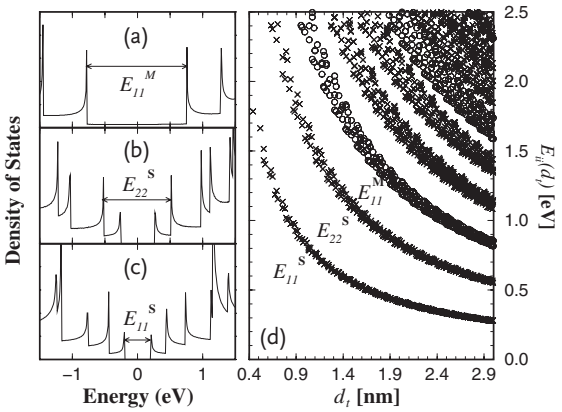

Figure 2.22 Density of electronic states for (a) an armchair (10, 10) SWNT, (b) a chiral (11, 9) SWNT, and (c) a zigzag (22, 0) SWNT obtained with the tight-binding model from [31]. (d) A plot (called a Kataura plot [113]) of the electronic transition energies E_{ii} for all the (n, m) SWNTs with diameters from 0.4 nm to 3.0 nm using a simple first-neighbor tight-binding model [31]. Deviations from this simple one-electron model are expected for the lower energy transitions E_{11}^S and for SWNTs with $d_t \lesssim 1\,\text{nm}$. Other corrections due to many-body interactions are also important [112].

which (n, m) carbon nanotubes can be in resonance with my laser line?" In other words, since the observable Raman spectra come predominantly from tubes in resonance with E_{laser}, Figure 2.22 specifies the nanotubes that will be observable for a given laser line.

Because of this resonance process, Raman spectra at the single nanotube level allow us to study the electronic and phonon structure of SWNTs in great detail. The E_{ii} vs. d_t plot shown in Figure 2.22d is called the "Kataura plot" in the literature (from [113]), and the early plots were made using a first-neighbor tight-binding model and the zone-folding procedure described in this chapter [31]. As we will see later, resonance Raman spectroscopy shows that the general trends seen in Figure 2.22d are correct, but for an accurate determination of the E_{ii} for each (n, m) SWNT, other effects must also be considered, as discussed briefly in Section 2.4, and in more detail in Chapter 10.

2.4 Beyond the Simple Tight-Binding Approximation and Zone-Folding Procedure

The simple tight-binding method used to describe electrons in a sp^2 system is pedagogic and gives a very good first-order approximation for the electronic structure of graphene and the other sp^2 nanocarbons. However, for an accurate description of the physical properties, other effects also have to be considered:

- Many-body effects, like electron–electron (e-e) and electron–hole (e–h) interactions have to be considered to describe the energy of excited states of graphene.
- These many-body effects such as excitonic (electron–hole) interactions become extremely important when one-dimensional quantum confinement takes place, thus having a strong influence on the optical properties and Raman spectra of carbon nanotubes and nanoribbons.
- Curvature in nanotubes and edge effects in nanoribbons will substantially change the electronic properties of these materials when their dimensions (diameter for tubes, width for ribbons) reach the nanometer scale.

These concepts will be discussed in detail elsewhere in the book. Here we expand briefly on the failure of the description given in Section 2.3 for small diameter SWNTs such as the (4, 2) carbon nanotube. Beyond this simple description, deviations from the simple linear approximation for the electronic dispersion relations of the graphene layer arise from the $\sigma - \pi$ hybridization of the electronic orbitals caused by the curvature of the nanotube wall [114]. Curvature-related effects introduce a band gap in the electronic dispersion relations at the Fermi level near the K and K' points in the Brillouin zone and this band gap affects the electronic band structure and physical properties in many ways. The curvature effect scales inversely with the square of nanotube diameter, being especially important for small diameter nanotubes, such as for the (5, 0) nanotube which becomes metallic. The simple π-band nearest neighbor tight-binding approximation used in Figure 2.17

is not able to describe curvature effects, since the description of nanotube curvature requires at least four orbitals per carbon atom, $2s, 2p_x, 2p_y, 2p_z$, as discussed in Chapter 10. Furthermore, next-nearest neighbor interactions also affect the electronic band structure of a graphene layer, not only in the vicinity of the K and K' points, as shown by comparing the nearest neighbor and the third nearest neighbor approximations with the results of *ab initio* electronic structure calculations [115]. Thus, Figure 2.17 does not reflect the real electronic band structure of a (4, 2) nanotube which still remains semiconducting, being a lowest order approximation in the limit of small diameter SWNTs where more detailed calculations are necessary. *Ab initio* calculations for a (4, 2) nanotube [108] yield an electronic band structure that is substantially different from the results obtained by the zone-folding scheme, as discussed in Chapter 10.

Problems

[2-1] Using Eq. (2.5), estimate the $1s$ energy of B, C and N atoms. In order to observe the core state energy, we usually use XPS (X-ray photoelectron spectroscopy) measurements. Explain how to measure $1s$ states for these atomic species by XPS with some illustrative figures.

[2-2] An electronic p orbital has angular momentum $\ell = 1$. Obtain the spherical harmonic $Y_{\ell m}(\theta, \phi)$ for $\ell = 1$ and $m = -1, 0, 1$. By combining these three functions, construct the p_x, p_y and p_z functions. Plot the shape of the p_x, p_y and p_z functions in three dimensions.

[2-3] Plot the rough shape of $R_{n\ell}(r)$ in Eq. (2.2) for $1s$, $2s$ and $2p$ states as a function of r. Explain how these functions are orthogonal to each other.

[2-4] When we change Z to $Z - 2$ in Eq. (2.5) for expressing the screening between two $1s$ electrons, estimate the $2s$ energy of B, C and N atoms.

[2-5] In order to solve Eq. (2.1), express the wavefunction as $\Psi(\boldsymbol{r}) = R(r)\Theta(\theta)\Phi(\phi)$ and obtain the equations for the variables of r, θ, and ϕ. Explain qualitatively why $2p$ orbitals have a higher energy than $2s$ orbitals. It is only for the case of the hydrogen atom that the $2s$ and $2p$ levels have an identical energy.

[2-6] Using the unitary matrix U in Eq. (2.16), diagonalize the Hamiltonian in Eq. (2.14).

[2-7] Solve the Schrödinger equation for the H molecule for the case that $s = \langle \Psi_1 | \Psi_2 \rangle$ is not zero. Obtain both eigenvalues and wavefunctions.

[2-8] Use the tight-binding model to obtain the electronic band structure for π electrons in polyacetylene. In the case of polyacetylene, there are two kinds of structures, the cis- and trans-structures (see Figure 2.23). In the case of trans-polyacetylene, the transfer integral t for π electrons should have two

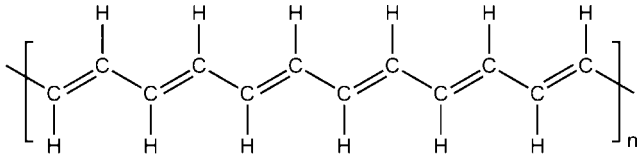

Figure 2.23 The structure of trans-polyacetylene, with alternative C–C bonds in the trans-configuration. In cis-polyactylene (not shown), an armchair edge shaped C–C chain appears.

values t_1 and t_2 depending on the double and single bond nature. Show that an energy gap which is proportional to $|t_1 - t_2|$ appears in the case of trans-polyacetylene.

[2-9] Obtain the coordinates in k space for the K, M, and Γ points and obtain the energy values for the simplest tight-binding energy for graphene at these high symmetry points in the Brillouin zone (Eq. (2.32)).

[2-10] Obtain Eqs. (2.33) and (2.34). Evaluate the value of the Fermi velocity.

[2-11] Show that the density of states is proportional to E when the energy dispersion is $E = a\sqrt{k_x^2 + k_y^2}$ in two-dimensional materials. How about for the linear dispersion in one-dimensional materials?

[2-12] Plot the density of states for the parabolic energy band, $E = a(k_x^2 + k_y^2)$.

[2-13] By expanding $f(k)$ of Eq. (2.28) near the K point, show that the Hamiltonian matrix is written by Eq. (2.35).

[2-14] Explain how to obtain the density of states for the cosine energy band, $E = a(\cos(k_x a) + \cos(k_y a))$ numerically.

[2-15] Calculate the diameter for an (n, m) SWNT. What are the values of the diameters for (5,5), (9,0), (10,5) SWNTs? What are possible (n, m) values for SWNTs having a 1.5 ± 0.02 nm diameter?

[2-16] For a given (n, m) SWNT, show the expression of $\boldsymbol{T} = (t_1, t_2)$ as a function of n, m. What is the length of $\boldsymbol{T}$?

[2-17] Show that $|\boldsymbol{a}_1 \times \boldsymbol{a}_2| = \sqrt{3}a^2/2$ and that the number of hexagons in the nanotube unit cell is $N = 2\left(n^2 + nm + m^2\right)/d_R$.

[2-18] Show the relation for an (n, m) SWNT $|\boldsymbol{C}_h \times \boldsymbol{T}| = \sqrt{3}a^2\left(n^2 + nm + m^2\right)/d_R$, where $d_R = \mathrm{gcm}(2n + m, 2m + n)$ and gcm is an integer function of the greatest common multiplier.

[2-19] Show the reciprocal lattice unit vectors $(\boldsymbol{K}_1, \boldsymbol{K}_2)$ as a function of n, m in 2D reciprocal space.

[2-20] Show that $|\boldsymbol{K}_1| = 2/d_t$ and $|\boldsymbol{K}_2| = 2\pi/|\boldsymbol{T}|$.

[2-21] Give the 1D electronic structure for the (10, 10) and (18, 0) SWNTs. Plot the cutting lines (1D Brillouin zone of SWNTs) in the 2D reciprocal space of the 2D Brillouin zone of graphene for these two SWNTs.

[2-22] Show that in Figure 2.18, $\boldsymbol{YK} = [(2n + m)/3]\boldsymbol{K}_1$, which is Eq. (2.39).

[2-23] Plot the cutting lines for type-I, type-II semiconducting and metallic SWNTs and show which cutting lines correspond to E_{11}^S, E_{22}^S, E_{33}^S, and E_{11}^M transitions for each case.